

A comparative study of the DSBGK and DVM methods for low-speed rarefied gas flows

Minh Tuan Ho^a, Jun Li^{b,*}, Lei Wu^a, Jason M. Reese^c, Yonghao Zhang^a

^a*James Weir Fluids Laboratory, Department of Mechanical and Aerospace Engineering,
University of Strathclyde, Glasgow G1 1XJ, UK*

^b*Center for Integrative Petroleum Research, College of Petroleum Engineering and Geosciences,
King Fahd University of Petroleum & Minerals, Saudi Arabia*

^c*School of Engineering, University of Edinburgh, Edinburgh EH9 3FB, UK*

Abstract

Low-speed rarefied gas flow in a lid-driven cavity is chosen as a test case in order to assess the accuracy and efficiency of both the Direct Simulation Bhatnagar-Gross-Krook (DSBGK) method and the Discrete Velocity Method (DVM) for solving the BGK kinetic equation. Various lid-speeds and a broad range of rarefaction levels, from slip to near free-molecular flows, are investigated. The DSBGK and DVM results are in satisfactory agreement for all the examined cases in 2D and 3D. As a statistical method, the stochastic noise of the DSBGK method is much smaller than that of the conventional Direct Simulation Monte Carlo (DSMC) method, and is independent of the Mach number. To achieve the required accuracy, the DSBGK simulations need more CPU time than the DVM simulations, i.e. for the 2D cases, a factor of 2 to 15 times more for convergence, and about 50 to 80 times more overall, including the time-averaging process. However, for 3D cases, the third direction in the DVM velocity grid is needed, so the computational cost of DSBGK is now only 0.16 to 0.51 times that of the DVM for the convergence process, and 1.6 to 5.8 times that of the DVM overall. The efficiency of the DSBGK method can also be expected to be enhanced in large-scale 3D simulations, where the computational cost for time-averaging becomes negligible in comparison with the convergence process. The DSBGK simulations require much less memory, even at low Mach numbers, than the DVM simulations; in the test cases with the required accuracy, about 10 simulated molecules per cell in the DSBGK simulations are sufficient for an arbitrary

*Corresponding author

Kn, while the DVM requires at least 4×24 and $4 \times 24 \times 12$ velocity grids for the 2D and 3D cases, respectively, even at $\text{Kn} = 0.1$. Finally, we discuss the ray effects of the DVM, which exist in flow problems with a discontinuous boundary and are caused by incompatibility of the velocity grid, the spatial grid, and the order of accuracy of the numerical scheme.

Keywords: Rarefied gas dynamics, Kinetic equation, Direct simulation BGK method, Discrete velocity method, Low speed flows, Ray effects

1. Introduction

When the mean free path of gas molecules becomes appreciable compared to the characteristic flow length, the conventional Navier-Stokes equations fail, and gas kinetic theory should be applied to study the rarefied gas dynamics. Low-speed rarefied gas flows are characteristic of both MEMS and tight porous media [1, 2]. While the Direct Simulation Monte Carlo (DSMC) method [3] is the most popular molecular-based technique for modelling rarefied flows [4, 5, 6], it is computationally expensive and essentially impractical for low-speed flows due to stochastic noise. For example, to find the gas permeability of porous media, a large pressure ratio is usually applied between the inlet and the outlet to increase the signal-to-noise ratio and hence reduce the sampling required [7, 8, 9]. In the near-continuum regime, however, the flow velocity is large, and the obtained permeability is very likely not independent of the pressure gradient because of the nonlinear Forchheimer effect. It is therefore important to develop efficient and accurate numerical methods in order to simulate low-speed rarefied gas flows.

The information-preservation (IP) DSMC is probably the first attempt to simulate low-speed flows efficiently [10]. In addition to the macroscopic quantities that can be obtained by conventional sampling, IP-DSMC introduces information quantities (such as the information velocity and information temperature) to reduce the statistical noise significantly. However, the evolution of these information quantities is ad-hoc; for example, the shear viscosity needs to be adjusted.

The Low-variance Deviational Simulation Monte Carlo (LVDSMC) solver has been proposed in Refs. [11, 12, 13]. In this method, computational efficiency is

24 significantly improved by simulating only the deviation from an equilibrium state.
25 Since the computational cost does not depend on the Mach number (Ma), rarefied
26 gas flows with Ma as low as 10^{-5} have been simulated. This is in sharp contrast
27 to DSMC, in which the required statistical sampling leads to a computational cost
28 that is proportional to Ma^{-2} [14]. LVDSMC has also been extended to solve the
29 linearized Bhatnagar-Gross-Krook (BGK) kinetic model equation [15, 16] and the
30 McCormack kinetic equation for binary gas mixtures [17]. Excellent agreement with
31 other deterministic solvers has been reported. There have been other reports of
32 stochastic techniques coupled with deterministic methods to reduce the variance of
33 particle methods [18, 19, 20, 21].

34 The Direct Simulation BGK (DSBGK) method is also a particle-based approach
35 and has been recently proposed for improving the efficiency of rarefied gas flow sim-
36 ulations at very low speeds [22]. It has been validated against DSMC simulations for
37 several benchmark problems over a wide range of Knudsen numbers (Kn , defined as
38 the ratio of the mean free path to the characteristic flow length) [23, 24]. Compared
39 with the standard DSMC technique, the DSBGK method achieves high efficiency
40 by avoiding generating a large number of random fractions in the intermolecular
41 collision process, and by using increments (instead of transient values) of molecular
42 variables to update macro quantities in each cell based on the conservation laws
43 of mass, momentum and energy. This updating algorithm significantly reduces the
44 stochastic noise due to discontinuous events of simulated molecules randomly mov-
45 ing into and out of cells. A comparative analysis of the algorithms of the DSMC
46 and DSBGK methods, with comparisons of simulation results produced by each, is
47 presented in Ref. [24].

48 The Discrete Velocity Method (DVM), on the other hand, deterministically solves
49 the Boltzmann equation, or simplified models [25, 26]. DVM has been widely used
50 to produce reliable data for rarefied gas flows from low to high speed [27, 28, 29].
51 Although the DVM offers accurate fluctuation-free solutions, it generally requires
52 high dimensionality in the distribution function, which may lead to a high demand
53 in computational memory and cost (although a memory reduction technique has
54 recently been proposed [30]). In addition to the dimensions in spatial space, the

55 DVM also usually needs three-dimensional discretization in molecular velocity space,
 56 whereas particle-based methods (such as DSMC and DSBGK) only need a number of
 57 simulated molecules per cell to dynamically discretize the molecular velocity space.
 58 For 1D and 2D flow problems, the dimensions of DVM in molecular velocity space
 59 can be reduced [31]. Moreover, if only the steady state solution is of interest, DVM
 60 can accelerate its rate of convergence by using implicit time-marching schemes or
 61 other iterative schemes [26, 32]. To the best of the authors' knowledge, particle-based
 62 methods usually have no such acceleration opportunities without losing accuracy,
 63 due to their time-evolutionary nature. Although the timestep Δt in the DSMC
 64 method is not restricted by the Courant-Friedrichs-Lewy (CFL) stability condition,
 65 the error in the transport coefficients has been found to be proportional to Δt^2 [33,
 66 34].

67 In this paper we assess the accuracy and computational efficiency of two different
 68 methods for solving the BGK kinetic equation — the DSBKG method and the DVM.
 69 Our chosen benchmark problems are the lid-driven cavity flows in 2D and 3D, which
 70 are characterized by shear-driven and flow compression phenomena that have been
 71 studied previously [35, 36, 37, 38, 39].

72 2. The BGK equation and its numerical solution

73 The Bhatnagar-Gross-Krook (BGK) kinetic model equation simplifies the Boltz-
 74 mann equation by using a relaxation-time approximation [15]. It can produce good
 75 results when thermal effects are negligible. Therefore, the relaxation time is chosen
 76 to recover only the shear viscosity, according to the Chapman-Enskog expansion in
 77 the continuum flow limit. Without an external body force, the BGK equation takes
 78 the following form:

$$\frac{\partial f}{\partial t} + \mathbf{c} \cdot \nabla f = -\frac{1}{\tau} (f - f_{\text{eq}}), \quad (1)$$

79 where $f = f(\mathbf{x}, \mathbf{c}, t)$ is the velocity distribution function of gas molecules with
 80 molecular velocity $\mathbf{c} = (c_x, c_y, c_z)$ at position $\mathbf{x} = (x, y, z)$ and time t , and f_{eq} is the
 81 equilibrium distribution function defined by the Maxwellian:

$$f_{\text{eq}} = \frac{n}{(2\pi k_B T/m)^{3/2}} \exp\left(-\frac{m\xi^2}{2k_B T}\right), \quad (2)$$

82 where n , m , T and k_B are the gas number density, molecular mass, temperature
83 and the Boltzmann constant, respectively; $\boldsymbol{\xi} = \mathbf{c} - \mathbf{u}$ is the peculiar velocity, with
84 \mathbf{u} the macroscopic flow velocity. Conservative flow variables $\mathbf{W} \equiv (n, n\mathbf{u}, ne)^T$ are
85 calculated as velocity moments of the distribution function, i.e.

$$\mathbf{W} = \int \boldsymbol{\psi} f d\mathbf{c}, \quad (3)$$

86 where $\boldsymbol{\psi} = (1, \mathbf{c}, c^2/2)^T$, and $e = (u^2 + 3k_B T/m)/2$ is the specific total energy.

87 The relaxation time τ in Eq. (1) is related to the dynamic viscosity μ and the
88 local pressure p by $\tau = \mu/p = \mu/(nk_B T)$. For gas molecules interacting through the
89 inverse power-law potential, the dynamic viscosity μ depends on the temperature T
90 as

$$\mu = \mu_0 \left(\frac{T}{T_0} \right)^\omega, \quad (4)$$

91 where ω is the viscosity index and μ_0 is the reference viscosity at the reference
92 temperature T_0 . For a lid-driven cavity flow, the reference temperature is chosen as
93 the bounding wall temperature $T_0 = T_w = 273$ K. Without loss of generality, argon
94 gas with $m = 6.63 \times 10^{-26}$ kg, $\mu_0 = 2.117 \times 10^{-5}$ Ns/m² and $\omega = 0.81$ is used here.

95 The mean free path λ_0 of gas molecules and the Knudsen number Kn are defined
96 as

$$\lambda_0 = \frac{\mu_0}{p_0} \sqrt{\frac{\pi k_B T_0}{2m}}, \quad \text{Kn} = \frac{\lambda_0}{L_{\text{char}}}, \quad (5)$$

97 respectively, where L_{char} is the characteristic length. The Mach number Ma is defined
98 as

$$\text{Ma} = \frac{u_w}{\sqrt{\gamma k_B T_0/m}}, \quad (6)$$

99 where γ is the specific heat ratio and u_w is the speed of the moving lid.

100 To fully determine the rarefied gas flow, the gas-surface interaction should be
101 specified. In this paper, we consider the Maxwell diffuse boundary condition at
102 the solid wall, i.e. the velocity distribution function for gas molecules entering the
103 computational domain is given by

$$f_{\text{B,diff}}(\mathbf{c}_r) = n_{\text{eff}} \left(\frac{m}{2\pi k_B T_w} \right)^{3/2} \exp \left(-\frac{m|\mathbf{c}_r|^2}{2k_B T_w} \right), \quad (7)$$

104 where \mathbf{c}_r is the reflected velocity of gas molecules relative to the wall, and the
105 effective number density n_{eff} is determined from the impermeable condition, that is,

106 the number of gas molecules moving to the wall is equal to that reflected from the
 107 same wall.

108 2.1. The DSBGK method

109 As the DSBGK method is a relatively new technique, some significant description
 110 is appropriate here. The DSBGK method for solving the BGK equation is proposed
 111 in Ref. [22], and further detailed in Ref. [24] where the extension to problems with
 112 an external body force is discussed. The simulation timestep Δt and computational
 113 domain cell size Δx are selected as in the DSMC method when simulating problems
 114 of high Kn. Each simulated molecule l carries four molecular variables: position
 115 \mathbf{x}_l , molecular velocity \mathbf{c}_l , number N_l of real molecules represented by the simulated
 116 molecule, and F_l that is equal to $f(\mathbf{x}_l, \mathbf{c}_l, t)$. The variables $n_{\text{tr},j}$, $\mathbf{u}_{\text{tr},j}$, $T_{\text{tr},j}$ of each cell
 117 j are updated using \mathbf{x}_l , \mathbf{c}_l and the *increment* of N_l based on the mass, momentum
 118 and energy conservation principles of the intermolecular collision process. They
 119 are then used in turn to update the molecular variables according to the BGK
 120 equation and an extrapolation of the acceptance-rejection scheme. The cell variables
 121 $n_{\text{tr},j}$, $\mathbf{u}_{\text{tr},j}$, $T_{\text{tr},j}$ are transitional variables and converge to n_j , \mathbf{u}_j , T_j that are defined
 122 by the moments of f , as discussed in Ref. [24] (after Eq. (13) in that paper).

123 At the initial state, \mathbf{x}_l and \mathbf{c}_l are selected according to the uniform initial dis-
 124 tribution $f_0 = f_{\text{eq},0}$, and the initial N_l is the same for all the simulated molecules
 125 (as in DSMC simulations). The initial F_l can then be determined accordingly, i.e.,
 126 $F_l = f_0(\mathbf{x}_l, \mathbf{c}_l, 0)$. In the simulation process, each simulated molecule l moves on a
 127 uniform trajectory until encountering boundaries. During each Δt , the trajectory of
 128 each simulated molecule may be divided into several segments by the cell interfaces.
 129 The time interval used by the simulated molecule l for the segment located inside
 130 the cell j is denoted by $\Delta_j t_l$. F_l can be updated by the integration of the BGK
 131 equation along each trajectory segment in sequence, i.e.

$$F_{l,\text{new}} = f_{\text{eq},j} + (F_l - f_{\text{eq},j}) \exp(-\Delta_j t_l / \tau), \quad (8)$$

132 where $f_{\text{eq},j}$ is the local equilibrium distribution defined by using the transient $n_{\text{tr},j}$,
 133 $\mathbf{u}_{\text{tr},j}$ and $T_{\text{tr},j}$ of the cell j .

134 According to an extrapolation of the acceptance-rejection scheme [22], $[\mathbf{x}_l, \mathbf{c}_l, N_l(f_2/f_1)_l]_{\text{all}}$
 135 is a representative sample of f_2 if $[\mathbf{x}_l, \mathbf{c}_l, N_l]_{\text{all}}$ is a representative sample of f_1 , where
 136 $(f_2/f_1)_l$ is the ratio of f_2 and f_1 at the point $(\mathbf{x}_l, \mathbf{c}_l)$. Thus, N_l can be updated
 137 according to F_l for each trajectory segment:

$$N_{l,\text{new}} = N_l F_{l,\text{new}} / F_l, \quad (9)$$

138 from which we obtain $\Delta_j N_l = N_{l,\text{new}} - N_l$ for the trajectory segment of the simulated
 139 molecule l located inside the cell j . This is the number increment of real molecules
 140 of class \mathbf{c}_l due to the intermolecular collisions inside the cell j during the current
 141 timestep. We compute the summation $\sum_{\epsilon_j} \Delta_j N_l$ over those trajectory segments
 142 located inside cell j during the current timestep. Mass conservation in the inter-
 143 molecular collision process inside cell j requires $\sum_{\epsilon_j} \Delta_j N_l = 0$. Thus, we reduce $n_{\text{tr},j}$
 144 if $\sum_{\epsilon_j} \Delta_j N_l > 0$ and then $\sum_{\epsilon_j} \Delta_j N_l$ will be reduced at the next timestep according
 145 to Eqs. (2), (8) and (9), and vice versa. This auto-regulation scheme ensures that
 146 $\sum_{\epsilon_j} \Delta_j N_l$ approaches zero. Similarly, $\sum_{\epsilon_j} (\Delta_j N_l m \mathbf{c}_l)$ and $\sum_{\epsilon_j} (\Delta_j N_l m \mathbf{c}_l^2 / 2)$ can be
 147 used to regulate $\mathbf{u}_{\text{tr},j}, T_{\text{tr},j}$ according to the momentum and energy conservations.
 148 The auto-regulation schemes used in the ordinary DSBGK simulations to update
 149 the cell variables after each timestep are therefore

$$\begin{aligned} n_{\text{tr},j}^{\text{new}} &= \frac{n_{\text{tr},j} V_j - \sum_{\epsilon_j} \Delta_j N_l}{V_j}, \\ \mathbf{u}_{\text{tr},j}^{\text{new}} &= \frac{n_{\text{tr},j} V_j \mathbf{u}_{\text{tr},j} - \sum_{\epsilon_j} (\Delta_j N_l \mathbf{c}_l)}{n_{\text{tr},j}^{\text{new}} V_j}, \\ T_{\text{tr},j}^{\text{new}} &= \frac{n_{\text{tr},j} V_j (3k_B T_{\text{tr},j} / 2 + m \mathbf{u}_{\text{tr},j}^2 / 2) - \sum_{\epsilon_j} (\Delta_j N_l m \mathbf{c}_l^2 / 2) - n_{\text{tr},j}^{\text{new}} V_j m (\mathbf{u}_{\text{tr},j}^{\text{new}})^2 / 2}{n_{\text{tr},j}^{\text{new}} V_j 3k_B / 2}, \end{aligned} \quad (10)$$

150 where V_j is the volume of cell j .

151 Now, we discuss how the DSBGK method reduces the stochastic noise in cell
 152 variables. When using particle-based methods to solve a kinetic equation, the ve-
 153 locity of each particle is usually updated independently according to the kinetic
 154 equation, which consequently satisfies the conservation laws on average but violates
 155 conservation during each timestep. The incurred stochastic noise due to this viola-
 156 tion can be reduced when solving the Boltzmann equation by using a special particle
 157 simulation method [40]. In this regard, the DSBGK method also adopts the special

158 scheme in Eq. (10) to impose conservations in each cell for each timestep to reduce
159 noise.

160 In addition to the noise caused by violation of conservation laws, there is another
161 type of noise in particle simulation due to frequent and random events of simulated
162 molecules moving into and out of each cell. The cell variables calculated by the
163 transient molecular variables inside the concerned cell therefore suffer from signif-
164 icant noise since the number of simulated molecules inside each cell on average is
165 small. This is the source of significant stochastic noise in DSMC and molecular
166 dynamic (MD) simulations. Instead of using transient values of molecular variables,
167 their increments along molecular trajectories are used in the DSBGK method to up-
168 date/regulate the cell variables. Although the molecular variables entering into each
169 cell are still random and noisy, by integrating the BGK equation along the molecular
170 trajectories, their variations are smooth. Consequently, noise in the cell variables
171 is significantly reduced by using Eq. (10) to update the cell variables, compared to
172 the DSMC and other particle simulation methods that define the cell variables by
173 using transient molecular variables.

174 At a wall boundary (with \mathbf{e}_n as the outward normal direction), \mathbf{c}_l and then F_l
175 are updated after molecular reflection at \mathbf{x}_l on the wall; N_l remains unchanged to
176 conserve mass. The reflected velocity \mathbf{c}_r is randomly selected, as in the DSMC
177 method, and then \mathbf{c}_l is updated to $\mathbf{c}_r + \mathbf{u}_w$, where \mathbf{u}_w is the wall velocity. (The
178 subscript l has been omitted for clarity in the notation of the incoming and reflected
179 velocities.)

180 We introduce $f_B(\mathbf{c})$ as the distribution function f at the reflection point \mathbf{x}_l at
181 time t in a local Cartesian reference frame moving at \mathbf{u}_w , so that $f_B(\mathbf{c}) = f(\mathbf{x}_l, \mathbf{c} +$
182 $\mathbf{u}_w, t)$. With an appropriate expression for $f_B(\mathbf{c})$, we then have $F_{l,\text{new}} = f_B(\mathbf{c}_r)$. The
183 distribution $f_B(\mathbf{c}_i)|_{\mathbf{c}_i \cdot \mathbf{e}_n < 0}$ of the incoming molecules is known from the molecular
184 information in the adjacent cell, and $f_B(\mathbf{c}_r)|_{\mathbf{c}_r \cdot \mathbf{e}_n > 0}$ is the distribution of reflected
185 molecules.

186 Theoretically, $f_B(\mathbf{c}_i)$ depends on the incoming molecules. When the wall velocity
187 is small, and to further reduce stochastic noise, a simple boundary condition is
188 proposed: we use cell variables rather than the molecular variables to determine

189 $f_B(\mathbf{c}_i)$ as a local equilibrium distribution, i.e.

$$f_{B,\text{simple}}(\mathbf{c}_i) = n_{\text{tr},j} \left(\frac{m}{2\pi k_B T_{\text{tr},j}} \right)^{3/2} \exp \left[\frac{-m(\mathbf{c}_i - (\mathbf{u}_{\text{tr},j} - \mathbf{u}_w))^2}{2k_B T_{\text{tr},j}} \right], \quad (11)$$

190 where $n_{\text{tr},j}$, $\mathbf{u}_{\text{tr},j}$, $T_{\text{tr},j}$ are the quantities of cell j close to the reflection point \mathbf{x}_l .

191 Then, the number flux of incoming molecules per unit wall area per unit time is:

$$\begin{aligned} N_{\text{in},\text{simple}} &= - \int_{\mathbf{c}_i \cdot \mathbf{e}_n < 0} f_{B,\text{simple}}(\mathbf{c}_i) (\mathbf{c}_i \cdot \mathbf{e}_n) d\mathbf{c}_i \\ &= n_{\text{tr},j} \sqrt{\frac{k_B T_{\text{tr},j}}{2\pi m}} \left[\exp(-\hat{u}_{\text{in}}^2) + \sqrt{\pi} \hat{u}_{\text{in}} (1 + \text{erf}(\hat{u}_{\text{in}})) \right], \end{aligned} \quad (12)$$

192 where $\hat{u}_{\text{in}} = -(\mathbf{u}_{\text{tr},j} - \mathbf{u}_w) \cdot \mathbf{e}_n / \sqrt{2k_B T_{\text{tr},j}/m}$. Similarly, the number flux N_{out} of
193 reflected molecules is:

$$\begin{aligned} N_{\text{out}} &= \int_{\mathbf{c}_r \cdot \mathbf{e}_n > 0} f_{B,\text{diffuse}}(\mathbf{c}_r) (\mathbf{c}_r \cdot \mathbf{e}_n) d\mathbf{c}_r \\ &= n_{\text{eff}} \sqrt{\frac{k_B T_w}{2\pi m}}. \end{aligned} \quad (13)$$

194 Now $N_{\text{out}} = N_{\text{in},\text{simple}}$ according to mass conservation, so we obtain an estimate for
195 n_{eff} :

$$n_{\text{eff},\text{simple}} = n_{\text{tr},j} \sqrt{\frac{T_{\text{tr},j}}{T_w}} \left[\exp(-\hat{u}_{\text{in}}^2) + \sqrt{\pi} \hat{u}_{\text{in}} (1 + \text{erf}(\hat{u}_{\text{in}})) \right]. \quad (14)$$

196 Then we update F_l by $F_{l,\text{new}} = f_{B,\text{diffuse}}(\mathbf{c}_r)$, where $n_{\text{eff}} = n_{\text{eff},\text{simple}}$. Compared to
197 the statistically accurate boundary condition that we develop below, this simple
198 boundary condition helps to reduce stochastic noise in the DSBGK simulations,
199 especially at low Ma. The numerical error incurred by the simple boundary will be
200 analyzed in Sections 3.1-3.3.

201 For closed flow problems, density drift has been observed in previous DSBGK
202 simulations after a large number of timesteps when using this simple implementation
203 of the boundary condition. To reduce the magnitude of the density drift, 2000
204 simulated molecules per cell are employed in the following study of 2D cavity flows.
205 However, the DSBGK accuracy is almost unchanged when using only 10 simulated
206 molecules per cell and more time-averaging samples. Correspondingly, the sampling
207 process of density could stop after only about 100 timesteps to avoid deviation
208 due to the slow density drift, because the transient density distribution has low
209 stochastic noise. In the following simulations, we will use only 100 samples for

210 number density n and larger number of samples for other macroscopic parameters,
 211 unless stated otherwise. Note that this unphysical density drift disappears when
 212 simulating open flow problems, because fixed number densities are applied at the
 213 open boundaries (e.g., the channel flow problem [24]). By contrast, flow velocity and
 214 temperature are not subject to unphysical drift, even in closed problems, thanks to
 215 the specified constraints at the boundary. Additionally, the density drift in closed
 216 problems becomes unnoticeable if the perturbation is very small (e.g. for the 2D
 217 cavity flow problem with $u_w = 10^{-6}$ m/s) [41].

218 If the flow velocity is not small (e.g. for the cavity flow problem with $u_w = 50$
 219 m/s), the density drift can be eliminated by using a statistically accurate boundary
 220 condition [41] in which the incoming number flux is directly calculated by using the
 221 information of incoming simulated molecules, although the correspondingly com-
 222 puted flux is noisy. As in the DSMC method, it is convenient for the DSBGK
 223 method to calculate the net flux $\Gamma(Q)$ of any molecular quantity $Q(\mathbf{c})$ in unit time
 224 and across unit area of the boundary surface, viz.

$$\Gamma(Q) = \frac{1}{\Delta t \Delta S} \sum_l N_l [Q(\mathbf{c}_i) - Q(\mathbf{c}_r)]_l, \quad (15)$$

225 where the summation is over the simulated molecules reflected on the sub-area ΔS
 226 during the current timestep Δt ; $Q(\mathbf{c}_i)$ and $Q(\mathbf{c}_r)$ are the incoming and reflected
 227 quantities, respectively. If $Q = m\mathbf{c}$ or $m\mathbf{c}^2/2$, then $\Gamma(Q)$ represents the stress or
 228 heat flux, respectively. Similarly, the incoming number flux is computed as:

$$N_{\text{in}} = \frac{1}{\Delta t \Delta S} \sum_l N_l. \quad (16)$$

229 As $N_{\text{out}} = N_{\text{in}}$ again, we obtain a statistically accurate formula for n_{eff} , i.e.

$$n_{\text{eff}} = \sqrt{\frac{2\pi m}{k_B T_w}} \frac{1}{\Delta t \Delta S} \sum_l N_l, \quad (17)$$

230 where $\sum_l N_l$ usually contains large stochastic noise. $F_{l,\text{new}} = f_{\text{B,diffuse}}(\mathbf{c}_r)$ is imple-
 231 mented to update F_l during the simulation process, and n_{eff} is updated by using
 232 Eq. (17) after each Δt .

233 The workflow of a DSBGK simulation can then be summarized as follows:

- 234 1. Initialization. Generate the domain cells and simulated molecules and assign
 235 them initial values for $n_{\text{tr},j}$, $\mathbf{u}_{\text{tr},j}$, $T_{\text{tr},j}$ and \mathbf{x}_l , \mathbf{c}_l , F_l , N_l , respectively.
- 236 2. Each simulated molecule l moves on a uniform trajectory until encountering
 237 boundaries. During each Δt , the trajectory of each simulated molecule may
 238 be divided into several segments by the cell interfaces. Then, \mathbf{x}_l , F_l , N_l are *de-*
 239 *terministically* updated along each segment in sequence. When encountering
 240 wall boundaries, \mathbf{c}_l is updated to $\mathbf{c}_r + \mathbf{u}_w$ according to the reflection model,
 241 and F_l is correspondingly updated to $f_B(\mathbf{c}_r)$. In open flow systems, simu-
 242 lated molecules are removed from the computational domain when they move
 243 across open boundaries, and new simulated molecules are generated at the
 244 open boundaries. The variables $n_{\text{tr},j}$, $\mathbf{u}_{\text{tr},j}$, $T_{\text{tr},j}$ of each cell j are updated at
 245 the end of each Δt .
- 246 3. After convergence, $n_{\text{tr},j}$, $\mathbf{u}_{\text{tr},j}$, $T_{\text{tr},j}$ provide the discrete solutions of the BGK
 247 equation at steady state.

248 2.2. The Discrete Velocity Method (DVM)

249 For a 2D case, two reduced velocity distribution functions are introduced to cast the
 250 3D molecular velocity space into 2D [26], i.e.

$$g = \int f(\mathbf{x}, \mathbf{c}, t) dc_z, \quad h = \int c_z^2 f(\mathbf{x}, \mathbf{c}, t) dc_z. \quad (18)$$

251 For convenience, in what follows we denote $\mathbf{c} = (c_x, c_y)$, $\boldsymbol{\xi} = (\xi_x, \xi_y)$ and $\mathbf{x} = (x, y)$.
 252 Using g and h , macroscopic variables can be computed as $n = \int g d\mathbf{c}$, $n\mathbf{u} = \int \mathbf{c}g d\mathbf{c}$,
 253 and $ne = \frac{1}{2} \int (c^2 g + h) d\mathbf{c}$. The governing equations for the two reduced distribution
 254 functions can be deduced from Eq. (1) in the form of the generic function $\phi = (h, g)$
 255 as

$$\frac{\partial \phi}{\partial t} + \mathbf{c} \cdot \nabla \phi = -\frac{\phi - \phi_{\text{eq}}}{\tau}, \quad (19)$$

where the reduced equilibrium distribution functions $\phi_{\text{eq}} = (h_{\text{eq}}, g_{\text{eq}})$ are

$$g_{\text{eq}}(\mathbf{x}, \mathbf{c}, t) = \int f_{\text{eq}}(\mathbf{x}, \mathbf{c}, c_z, t) dc_z = \frac{nm}{2\pi k_B T} \exp\left[-\frac{m\xi^2}{2k_B T}\right], \quad (20a)$$

$$h_{\text{eq}}(\mathbf{x}, \mathbf{c}, t) = \int c_z^2 f_{\text{eq}}(\mathbf{x}, \mathbf{c}, c_z, t) dc_z = k_B T g_{\text{eq}}/m. \quad (20b)$$

256 DVM is one of the most common deterministic approaches for solving the Boltz-
 257 mann equation and its simplified models [25, 26]. It projects the continuous molec-
 258 ular velocity space \mathbf{c} into a set of fixed N_c discrete velocities $\mathbf{c}^{(ii)}$ ($ii = 1, 2, \dots, N_c$).
 259 As a result, for the BGK model, the governing equation (19) is replaced by a system
 260 of N_c independent equations. Here, we discretize this system in time by a fully
 261 time-implicit Godunov-type scheme [26, 32]:

$$\begin{aligned} \left[\frac{1}{\Delta t^{(ts)}} + \mathbf{c}^{(ii)} \cdot \nabla + \frac{1}{\tau^{(ts)}} \right] \Delta \phi^{(ts)} &= \text{RHS}^{(ts)}, \\ \text{RHS}^{(ts)} &= \frac{1}{\tau^{(ts)}} [\phi_{\text{eq}}^{(ts)} - \phi^{(ts)}] - \mathbf{c}^{(ii)} \cdot \nabla \phi^{(ts)}, \end{aligned} \quad (21)$$

262 where $\Delta \phi^{(ts)} = \phi^{(ts+1)} - \phi^{(ts)}$ needs to be determined at the timestep ts . $\text{RHS}^{(ts)}$ is
 263 the explicit part, and the spatial derivative is approximated by a third-order upwind
 264 scheme. For instance, the derivative with respect to the x -direction at point x_{jj} is
 265 evaluated by:

$$\left. \frac{\partial \phi^{(ts)}}{\partial x} \right|_{jj} = \begin{cases} (2\phi_{jj+1}^{(ts)} + 3\phi_{jj}^{(ts)} - 6\phi_{jj-1}^{(ts)} + \phi_{jj-2}^{(ts)}) / (6\Delta x), & c_x^{(ii)} > 0, \\ (-2\phi_{jj-1}^{(ts)} - 3\phi_{jj}^{(ts)} + 6\phi_{jj+1}^{(ts)} - \phi_{jj+2}^{(ts)}) / (6\Delta x), & c_x^{(ii)} < 0. \end{cases} \quad (22)$$

266 The left-hand side of Eq. (21) is the implicit part, and the spatial derivative is
 267 approximated by a first-order upwind scheme. By marching in the appropriate
 268 direction, e.g. increasing x in the case of $c_x^{(ii)} > 0$, the unknown $\Delta \phi^{(ts)}$ can be
 269 obtained directly without solving a system of equations.

270 Note that Δt in Eq. (21) is a pseudo-timestep that is defined by the CFL con-
 271 dition, i.e. $\Delta t = \eta \Delta x^{\min} / c_x^{\max}$, where η is the CFL number, Δx^{\min} is the minimum
 272 spatial grid size, and c_x^{\max} is the maximum discrete speed. While η here can be
 273 smaller than 1 to capture transient behaviour, it can also be set as large as 10^4 (as
 274 it is in the studies below) to obtain a steady-state solution.

275 In order to evaluate the flow variables in Eq. (3), the product Gaussian quadra-
 276 tures in the velocity polar coordinates $\mathbf{c} = (c_p \cos \varphi, c_p \sin \varphi)$ and the velocity spher-
 277 ical coordinates $\mathbf{c} = (c_p \sin \theta \cos \varphi, c_p \sin \theta \sin \varphi, c_p \cos \theta)$ are used for 2D and 3D sim-
 278 ulations, respectively [36, 42]. For example, the flow variables in the 3D case are

279 approximated as:

$$\mathbf{W} = \int_0^\infty \int_0^{2\pi} \int_0^\pi \psi f c_p^2 \sin \theta d\theta d\varphi dc_p \approx \sum_{k=1}^{N_{c_p}} \sum_{j=1}^{N_\varphi} \sum_{i=1}^{N_\theta} w_{c_p}^{(k)} w_\varphi^{(j)} w_\theta^{(i)} \mathbf{F}(c_p^{(k)}, \varphi^{(j)}, \theta^{(i)}), \quad (23)$$

280 where $\mathbf{F} = \psi f c_p^2 \exp(c_p^2)$; N_{c_p} , N_φ and N_θ are the numbers of discretized points in
 281 the radius c_p , azimuth φ and inclination θ , respectively, of the velocity space; $c_p^{(k)}$
 282 and $w_{c_p}^{(k)}$ are the half-range Gauss-Hermite abscissae and weights, while $\cos \theta^{(i)}$ and
 283 $w_\theta^{(i)}$ are the Gauss-Legendre abscissae and weights in $[-1, 1]$ [43, 44]. The nodes $\varphi^{(j)}$
 284 are uniformly spaced on $[0, 2\pi]$ and $w_\varphi^{(j)} = 2\pi/N_\varphi$. We denote the total number of
 285 velocity grid points by $N_c = N_{c_p} \times N_\varphi$ and $N_c = N_{c_p} \times N_\varphi \times N_\theta$ for 2D and 3D
 286 velocity grids, respectively.

287 Our simulations start from the global equilibrium state. The convergence crite-
 288 rion for the steady-state, which is based on the velocity flow field, is checked every
 289 timestep as follows:

$$E(t) = \frac{\sum |\mathbf{u}(t) - \mathbf{u}(t - \Delta t)|}{\sum |\mathbf{u}(t)|} < 10^{-6}. \quad (24)$$

290 3. 2D cavity flows

291 As our first test case for comparison of the DSBGK method and the DVM, we
 292 consider the rarefied gas flow inside a square cavity of size $L = 1 \mu m$ and this size
 293 is used as the characteristic length $L_{\text{char}} = L$. Cartesian coordinates are used, with
 294 the origin located at the bottom left corner of the cavity, as shown in Fig. 1 (a), in
 295 which $X = x/L$ and $Y = y/L$. From the origin, the positive X - and Y -directions
 296 point towards the bottom right corner and the top left corner, respectively. The top
 297 lid moves in the positive X -direction with a constant speed u_w . The cavity walls
 298 are maintained at a constant temperature $T_w = T_0$.

299 Lid-driven cavity flows in 2D are simulated by both the DSBGK method and
 300 the DVM over a wide range of Knudsen and Mach numbers. We choose the lid
 301 speeds to be $u_w = 0.001, 1, 10, \text{ and } 50 \text{ m/s}$, which correspond to $\text{Ma} = 3.2 \times 10^{-6},$
 302 $3.2 \times 10^{-3}, 3.2 \times 10^{-2}, \text{ and } 0.16$, respectively. We also choose $\text{Kn} = 0.1, 1 \text{ and } 8$, to
 303 cover the slip, transition, and free-molecular flow regimes, respectively. Initially, the
 304 gas is in global equilibrium described by Eq. (2), with zero flow velocity and uniform

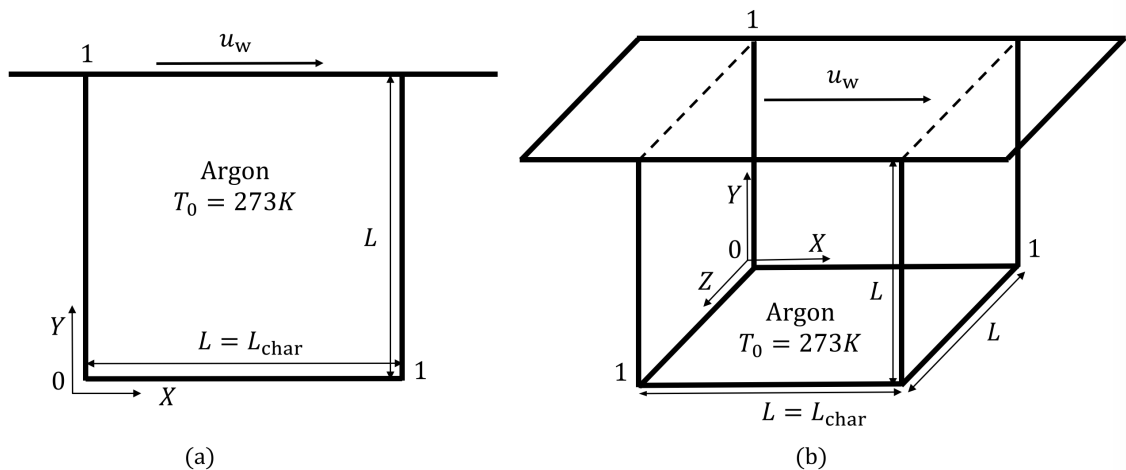


Figure 1: Schematic of the flow test cases: (a) 2D lid-driven cavity, (b) 3D lid-driven cavity.

305 temperature T_0 . The uniform number density is adjusted to obtain the desired value
 306 of Kn.

307 Unless stated otherwise, the number of uniform spatial cells/grids is 60^2 for both
 308 the DSBGK and the DVM simulations. For simplicity of comparison between the
 309 two methods, uniform spatial grids are implemented in this study. However, DVM
 310 can be easily extended to non-uniform grids [45], and DSBGK is unchanged when
 311 using non-uniform grids [24]. We use an 8×80 velocity grid in the DVM, and em-
 312 ploy 2000 simulated molecules per cell in the DSBGK method with the statistically
 313 accurate boundary condition Eq. (17) (or the simple boundary condition Eq. (14))
 314 for $Ma = 0.16$ (or for $Ma < 0.16$). The DSBGK simulations need 500 samples to
 315 smooth the results **for arbitrary Ma and Kn**. Coarser spatial and velocity grids (or
 316 smaller numbers of simulated molecules per cell) will be tested in Section 3.4 below.
 317 Note that the DSBGK simulations use dimensional quantities, while the DVM sim-
 318 ulations employ only dimensionless quantities scaled by a relevant reference value,
 319 e.g. $L_{\text{char}}, n_0, u_w, T_0$. Perturbed macroscopic quantities obtained by the two methods
 320 are reported in our results below, i.e.

$$\tilde{n} = \frac{n - n_0}{n_0}, \quad \tilde{u} = \frac{u}{u_w}, \quad \tilde{v} = \frac{v}{u_w}, \quad \tilde{T} = \frac{T - T_0}{T_0}, \quad (25)$$

321 where u and v are the components in the X and Y directions, respectively, of the
 322 macroscopic velocity vector $\mathbf{u} = (u, v)$. (Hereafter, the tildes on these perturbed
 323 macroscopic quantities are omitted for simplicity.)

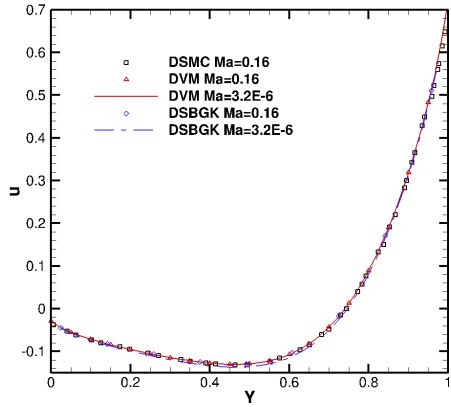
324 *3.1. Validation*

325 Figure 2 shows DVM, DSBGK and published DSMC [37] profiles of the perturbed u
326 and v velocity components along the vertical centreline ($X = 0.5$) and the horizontal
327 centreline ($Y = 0.5$), respectively, for various Ma and Kn. Figures 2 (a),(c),(e) show
328 that the velocity slip at the moving lid increases considerably with Kn, while the
329 increase at the bottom wall is negligible. For a moderate Mach number of 0.16, where
330 heat flux is insignificant, the DVM and DSBGK (with the statistically accurate
331 boundary condition) results agree very well with the published DSMC data [37] for
332 Kn = 0.1, 1 and 8, in which the variable hard-sphere (VHS) molecular model with
333 $\omega = 0.81$ was used.

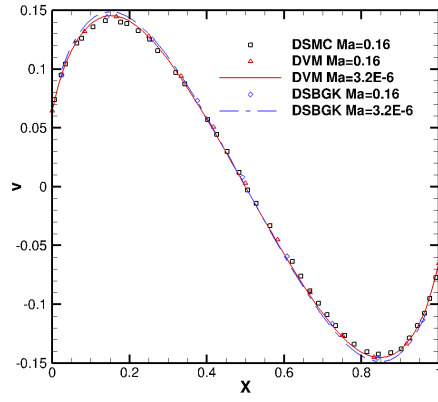
334 For Ma < 0.16, the DSBGK results obtained using the statistically accurate
335 boundary condition are dominated by stochastic noise (not shown here), so the
336 simple but smooth boundary condition is used instead. Consequently, the DSBGK
337 results have a small discrepancy from the DSMC data. Compared with the DVM
338 method in solving the same BGK equation, the maximum discrepancy in the u
339 profiles between the DVM and DSBGK methods is about 7.5% at Ma = 3.2×10^{-6} ,
340 Kn = 1, and occurs only in the flow region with relatively small perturbation.

341 Similarly, Figs. 2 (b),(d),(f) show that the v profiles obtained by the two methods
342 are in good agreement with the DSMC data at Ma = 0.16, Kn = 0.1, 1 and 8. The v
343 profiles resemble a cosine function, with one maximum and one minimum near the
344 left and right walls, respectively. These extrema are almost anti-symmetrical with
345 respect to the cavity centre; this has also previously been shown using the linearized
346 kinetic equation [46]. As the Mach number decreases, the v profile remains nearly
347 unchanged in the DVM results, while a small discrepancy is observed in the DSBGK
348 results due to the use of the simple boundary condition. The maximum discrepancy
349 in the v profiles between the DVM and DSBGK methods is approximately 2.5% at
350 Ma = 3.2×10^{-6} and Kn = 0.1.

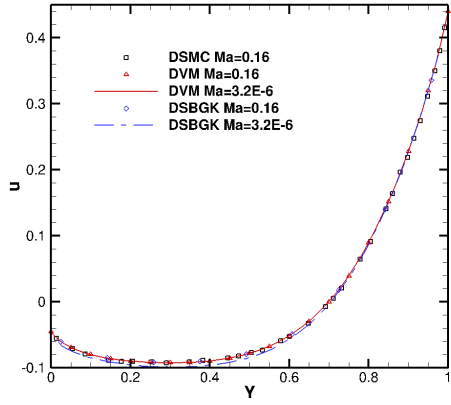
351 Note that it has been reported independently in Ref. [37] (see Fig. 4 of that
352 paper) that the u profile is independent of Ma, and the v profile remains essentially
353 unchanged with Mach number for Ma ≤ 0.32 . This is confirmed by the present
354 DVM and DSBGK results. Although not shown here, the u and v profiles produced



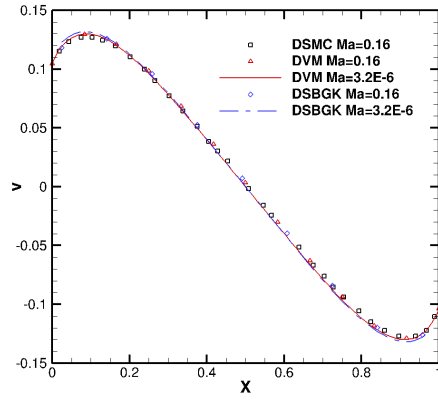
(a) u at $Kn=0.1$



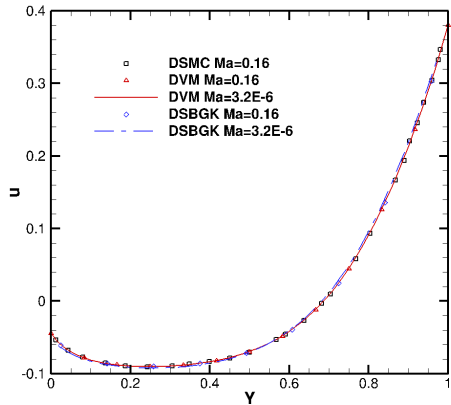
(b) v at $Kn=0.1$



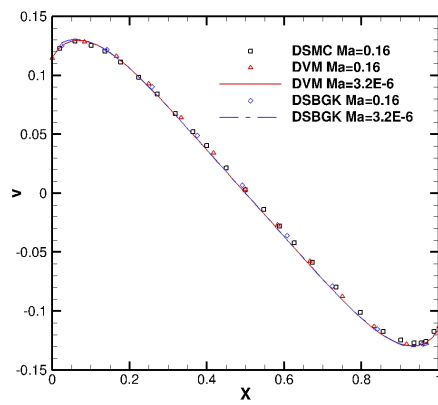
(c) u at $Kn=1$



(d) v at $Kn=1$



(e) u at $Kn=8$



(f) v at $Kn=8$

Figure 2: Profiles of the perturbed horizontal velocity u (left column) and perturbed vertical velocity v (right column) along the vertical centreline ($X = 0.5$) and horizontal centreline ($Y = 0.5$), respectively, of the 2D lid-driven cavity. The DVM and DSBGK results are compared with published DSMC data [37]. Note that the flow velocity has been normalized by the lid velocity u_w .

355 by the DVM and DSBGK simulations for $\text{Ma} = 3.2 \times 10^{-2}$ and 3.2×10^{-3} are
356 indistinguishable from those for $\text{Ma} = 3.2 \times 10^{-6}$.

357 *3.2. Effect of Mach number*

358 The impact of Mach number is investigated by fixing $\text{Kn} = 1$ and producing simu-
359 lations for $\text{Ma} = 3.2 \times 10^{-6}$, 3.2×10^{-3} , 3.2×10^{-2} , and 0.16. DSMC results are,
360 to the knowledge of the authors, not available in the literature for low-Ma flows,
361 except results for $\text{Ma} = 0.16$ that have been included in Fig. 2. We therefore use the
362 accurate DVM results as reference data, which are obtained using an 8×80 velocity
363 grid.

364 In Figs. 3 and 4, we find that the values of u and v remain almost constant for all
365 examined Ma, except their minima slightly increase for $\text{Ma} = 0.16$. The maximum
366 u is located at the centre of the top wall, and u is negative in the major part of the
367 cavity near the bottom, left and right walls. The positive and negative regions of v
368 are found toward the left and right walls, respectively, and the extrema are located
369 just under the top corners.

370 The u and v contour lines obtained by both the DVM and DSBGK simulations
371 are identical at $\text{Ma} = 0.16$, in which the DSBGK uses the statistically accurate
372 boundary condition, but are noticeably different at lower Mach numbers, in which
373 the DSBGK uses the simple boundary condition. The maximum discrepancies are
374 about 7.5% for u along $X = 0.5$, and 1.0% for v along $Y = 0.5$, at $\text{Ma} = 3.2 \times 10^{-6}$.
375 The maximum discrepancies for the n and T profiles along the horizontal centerline,
376 which are observed near the walls at $\text{Ma} = 3.2 \times 10^{-6}$, are 4.7% and 2%, respectively.

377 The contours of n are shown in Fig. 5. The gas is compressed and expanded near
378 the top right and top left corners, respectively, causing a respective rise and fall in n
379 at the top corners. The magnitude of the maximum and minimum in the n contours
380 increases with Ma as the gas compression and expansion become stronger at higher
381 lid speeds. The DVM and DSBGK results only differ slightly in their predicted n
382 for all Ma.

383 The T contour plots in Fig. 6 show that the hot and cold regions in the flow field
384 are toward the top right (gas compression) and top left (gas expansion) corners,
385 respectively. Similar to the dependence of n on Ma, the maximum and minimum

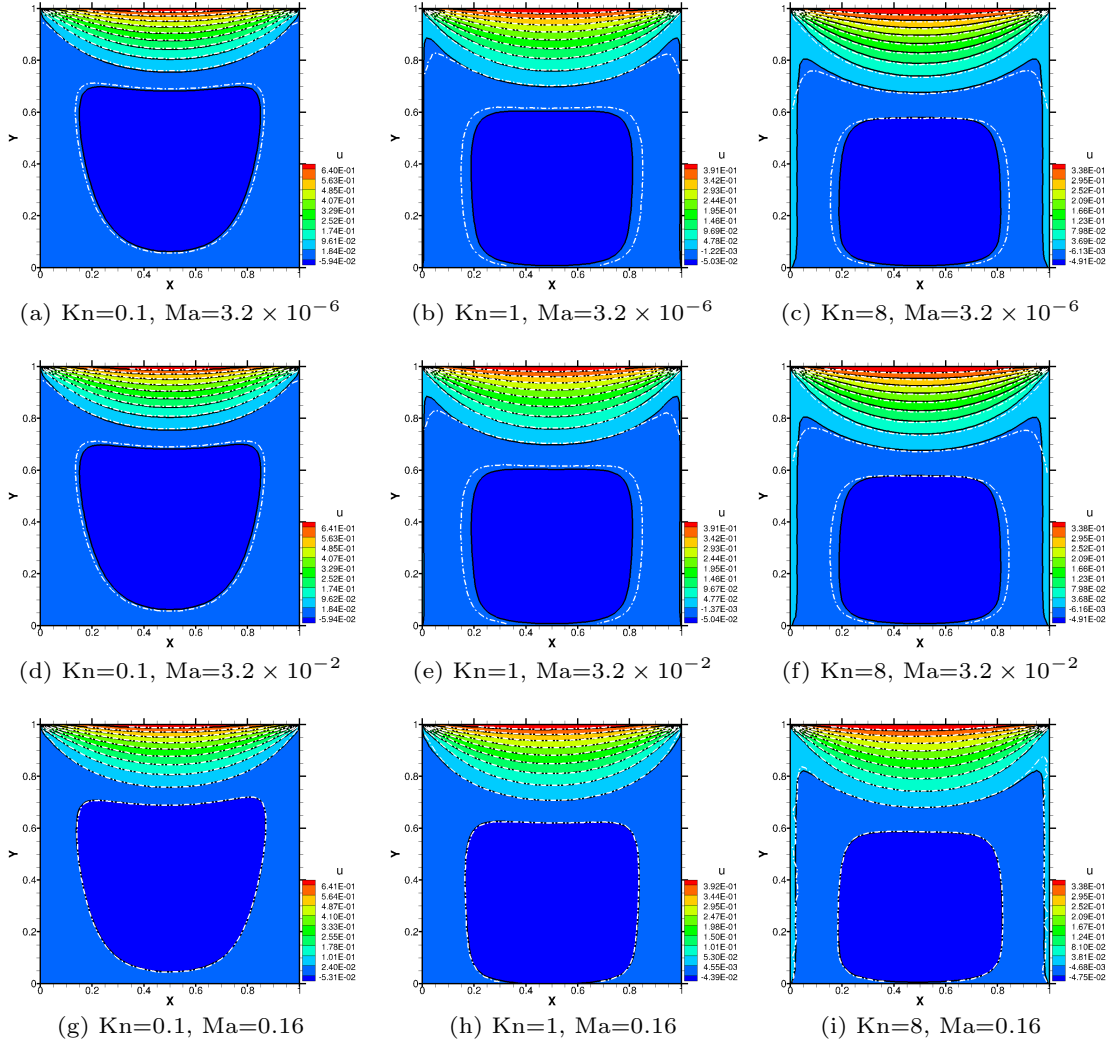


Figure 3: Contours of the perturbed horizontal velocity u in the 2D lid-driven cavity flow obtained using the DVM (the black solid line and coloured background) and the DSBGK method (the white dash-dot line).

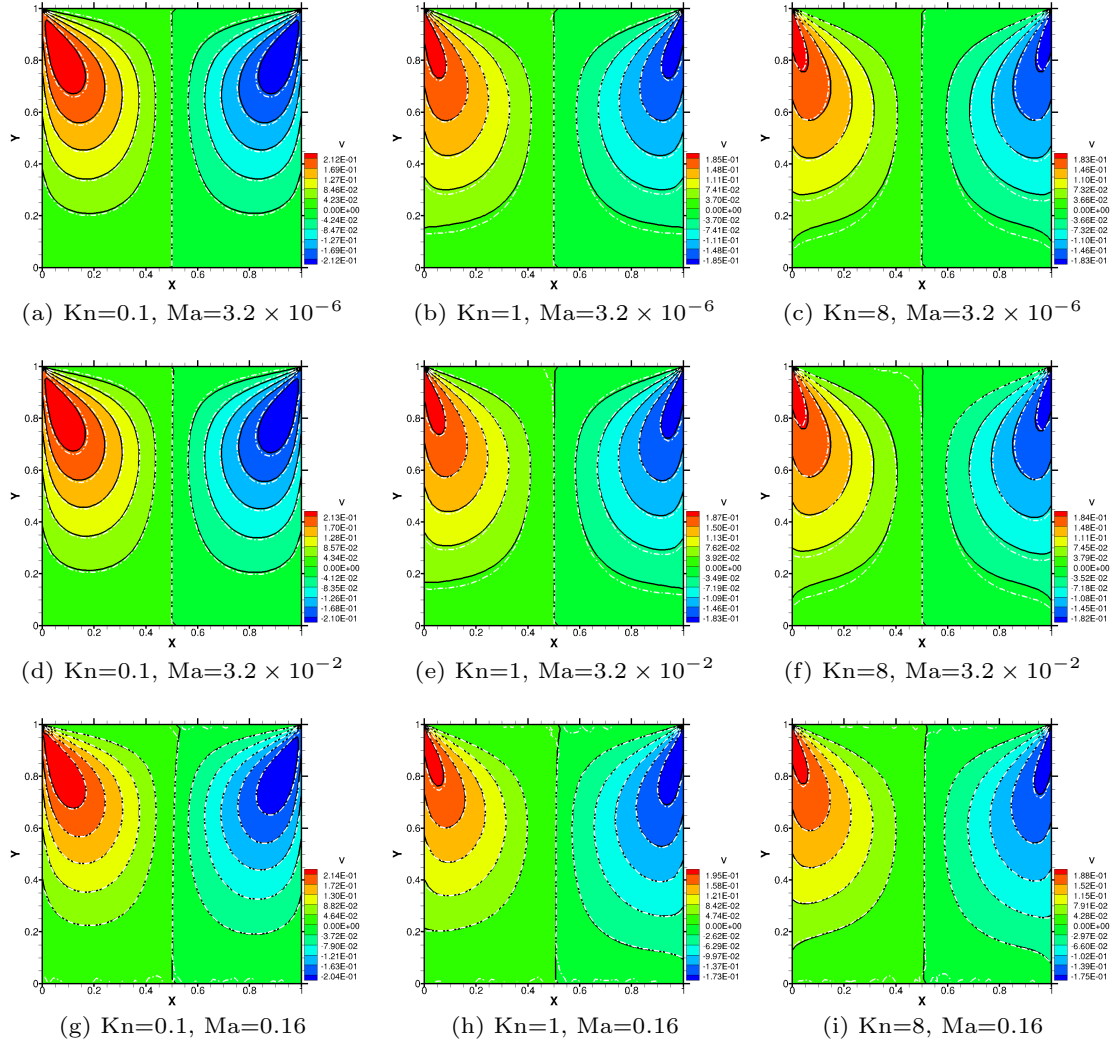


Figure 4: Contours of the perturbed vertical velocity v in the 2D lid-driven cavity flow obtained using the DVM (the black solid line and coloured background) and the DSBGK method (the white dash-dot line).

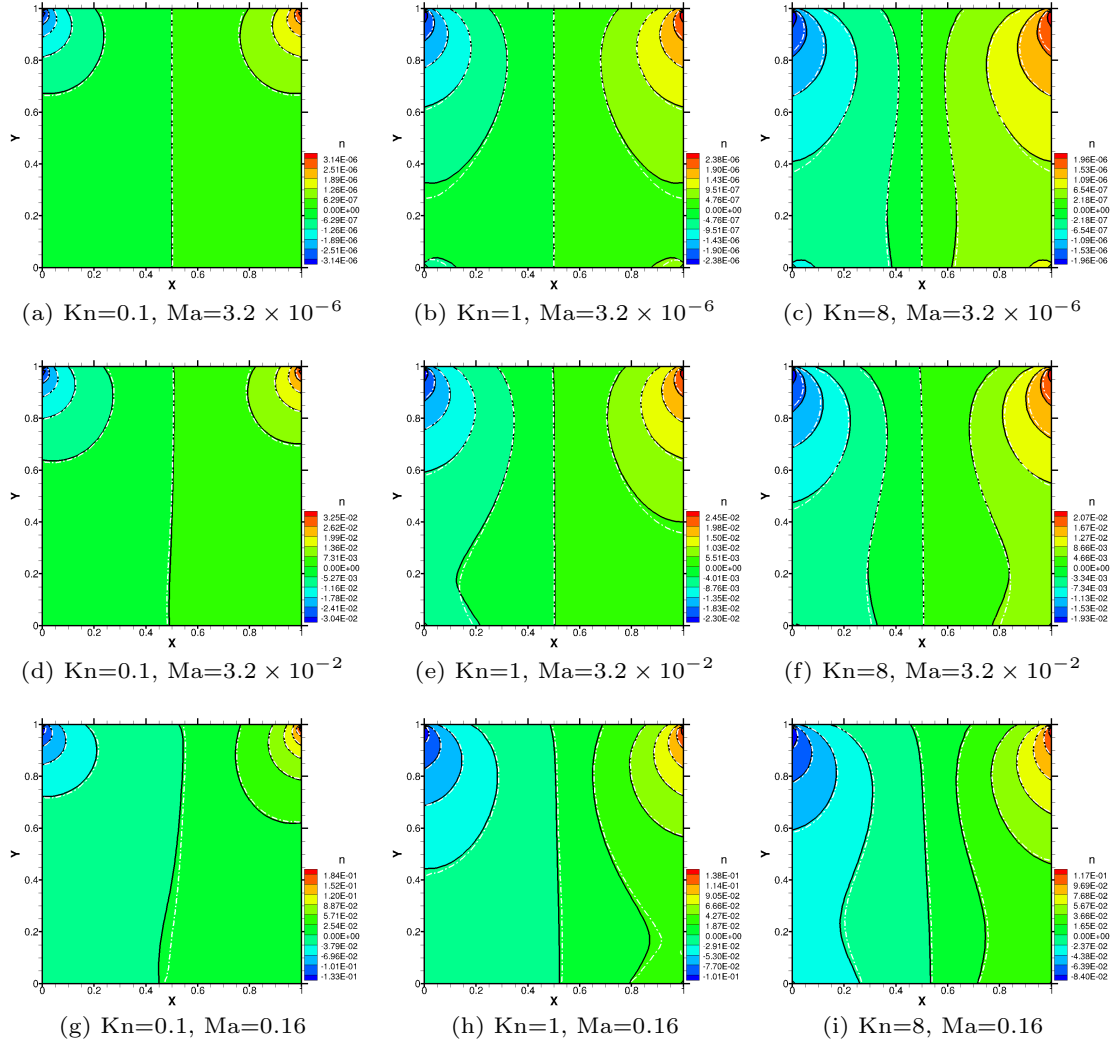


Figure 5: Contours of the perturbed number density n in the 2D lid-driven cavity flow obtained using the DVM (the black solid line and coloured background) and the DSBGK method (the white dash-dot line).

386 temperatures near the top corners also vary with Ma . However, unlike with n , these
 387 significant variations of T are not confined to the top corners as the Mach number
 388 increases. Instead, the hot region expands leftward, while the cold region draws in
 389 towards the left and extends downwards. The T distributions produced by the DVM
 390 and DSBGK methods are generally in good agreement with each other for all Ma .

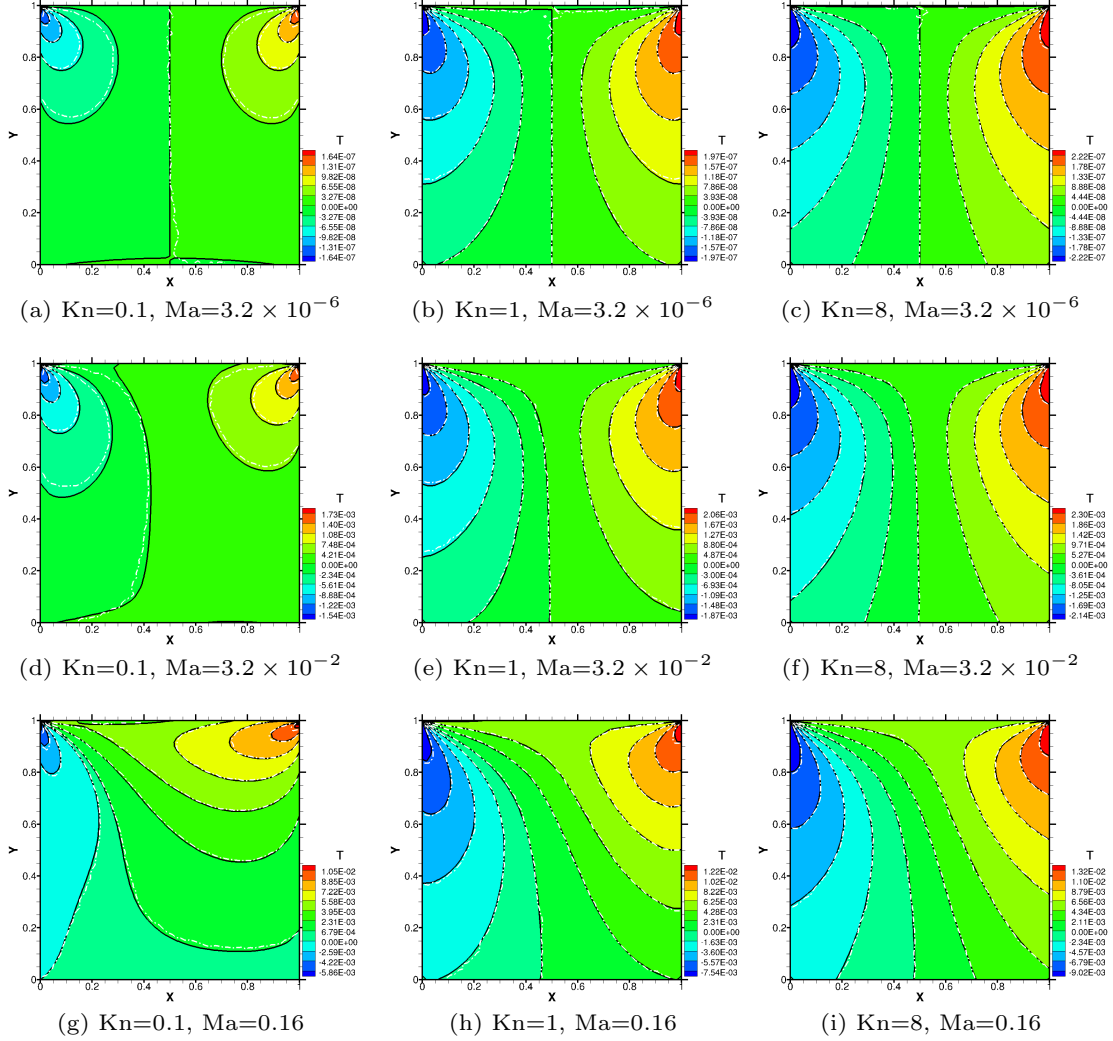


Figure 6: Contours of the perturbed temperature T in the 2D lid-driven cavity flow obtained using the DVM (the black solid line and coloured background) and the DSBGK method (the white dash-dot line).

391 3.3. Effect of Knudsen number

392 To assess the effects of rarefaction, we compare our simulation results at $Ma =$
 393 3.2×10^{-2} , and Knudsen numbers $Kn = 0.1, 1$ and 8 . The macroscopic flow fields

394 are presented in subfigures d), e) and f) of Figs. 3 to 6. Although the u and v
 395 flow patterns remain almost unchanged, the magnitudes of u and v decline with
 396 increasing Kn. For Knudsen numbers increasing from 0.1 to 8, the magnitude of the
 397 maximum (minimum) u reduces around 47% (17%); for v , it is about 14% (13%).

398 Likewise, the magnitudes of the maxima and minima in the n field decrease with
 399 increasing Kn. From $\text{Kn} = 0.1 \rightarrow 8$, the magnitudes of the maximum and minimum
 400 of n reduce by about 37%. The regions of low and high n also expand downward with
 401 increasing Kn. The temperature in the hottest (coldest) region increases (decreases)
 402 by 33% (39%) as the Knudsen number rises from 0.1 to 8.

403 Using the simple boundary condition in DSBGK produces very good agreement
 404 with DVM for n and T contours at all Kn. The u and v contours of DSBGK deviate
 405 slightly from those of DVM at $\text{Kn} = 1, 8$, and this deviation diminishes at $\text{Kn} = 0.1$.

406 3.4. *Effects of velocity and spatial grids, and computational costs*

407 So far, we have focused on the accuracy of the DVM and DSBGK methods at
 408 different Kn and Ma using either a high resolution velocity grid or a large number of
 409 simulated molecules per cell. For practical applications, it is important to strike a
 410 balance between computational accuracy and efficiency. So we test different reduced
 411 velocity grids in the DVM simulations and reduced numbers of simulated molecules
 412 per cell in the DSBGK simulations, for $\text{Ma} = 3.2 \times 10^{-3}$ and $\text{Kn} = 0.1, 1$ and 8. The
 413 simple boundary is again used to stabilize the DSBGK simulations. The timestep
 414 in the DSBGK simulations is fixed at $\Delta t = 2.0\Delta x\sqrt{m/(2k_{\text{B}}T_0)}$ for different Kn to
 415 clarify the relation between the timesteps and the corresponding CPU simulation
 416 time, **which is the wall clock time for both DVM and DSBGK simulations, unless**
 417 **stated otherwise.**

418 Allowing tolerances of a maximum local relative deviation (from the accurate
 419 DVM results obtained with an 8×80 velocity grid) of 10% in u, v, n, T profiles along
 420 the horizontal centreline, the velocity grids of the DVM method can be reduced to
 421 $4 \times 24, 4 \times 40, 4 \times 48$ at $\text{Kn} = 0.1, 1, 8$, respectively, while the number of simulated
 422 molecules per cell in the DSBGK method can be decreased to 10 for all Kn. Figures
 423 7 to 9 show the contours of macroscopic quantities obtained by the DVM and the

424 DSBGK using these numerical parameters, alongside the reference contours obtained
425 by the DVM with an 8×80 velocity grid.

426 The accuracy of the DSBGK method does not deteriorate when using only 10
427 simulated molecules per cell, except for a small drift in the density distribution.
428 However, the stochastic noise is significantly increased, so 5000 samples are needed
429 to smooth the results. Although the number of simulated molecules per cell used by
430 the DSBGK method is small, the molecular velocities inside each cell are dynam-
431 ically updated via the frequent and random events of simulated molecules moving
432 into and out of each cell (from the perspective of the Eulerian description). The
433 molecular velocities along all representative trajectories are also dynamically up-
434 dated via the frequent and random molecular reflections at the boundary (from
435 the perspective of the Lagrangian description). Thus, the *dynamic* discretization
436 of using few simulated molecules per cell in the DSBGK method can sample from
437 the whole velocity space and therefore allow as fine discretization of the unbounded
438 molecular velocity space as desired with the increase of simulation time. This is the
439 same as in the DSMC method.

440 The DVM contours with coarse velocity grids can be seen to oscillate around the
441 reference solutions in the regions far from the two top corners. This can be explained
442 as “ray effects”, which are known as major shortcomings of the DVM when applied to
443 neutron transport and radiative transfer problems involving discontinuous boundary
444 conditions [47, 48, 49]. These effects are due to the finite discretization of velocity
445 space tending to capture discontinuities, whereas the finite discretization of spatial
446 space tending to smooth the flow field. The velocity grid therefore should be fine
447 enough so that the error due to ray effects can be compensated by the error due
448 to numerical diffusion, which is related to the spatial grid and spatial discretization
449 scheme [50].

450 In Fig. 10, the ray effects (wavy contours) can be clearly observed in the DVM
451 solution with a 60^2 spatial grid and a 4×40 velocity grid, for the case of $\text{Ma} =$
452 3.2×10^{-3} , $\text{Kn} = 8$. The effects are diminished by increasing the velocity grid to
453 4×80 , by reducing the spatial grid to 30^2 , or by using a lower-order scheme, i.e. a
454 first order upwind scheme, rather than Eq. (22). The contours obtained by the first

455 two options are almost identical to each other (and to the reference contours shown
 456 in Fig. 9) and slightly differ from the results using the third option. Among these
 457 three options for this case of high Kn, the second option, i.e. compatible coarse
 458 velocity and spatial grids with a high-order upwind scheme, provides accurate data
 459 at relatively cheap computational cost.

460 In addition to velocity grid size, the layout of velocity grid is also important to
 461 mitigate ray effects. For instance, a 32^2 velocity grid in Cartesian coordinates yields
 462 significant ray effects, whereas a 4×80 velocity grid in polar coordinates (about
 463 one-third size of the Cartesian grid) does not. These ray effects are sensitive to N_φ
 464 but not to N_{c_p} , e.g. a 4×80 velocity grid can provide an identical solution to an
 465 8×80 velocity grid (see Figs. 9 and 10).

466 In addition, Figs. 7 to 9 show that ray effects increase with Knudsen number,
 467 since the collision process is dominated by the streaming process. To mitigate ray
 468 effects when a linearized kinetic equation is used, the perturbed distribution func-
 469 tion can be split into two parts: the part induced by the wall velocity can be solved
 470 analytically along characteristic directions, whereas the other part is solved numer-
 471 ically [36].

472 It is also important to compare the computational costs of the DVM and DSBGK
 473 methods in achieving the required solution tolerances. A comparison of computa-
 474 tional costs is given in Table 1. All the serial calculations are performed using a
 475 single CPU core on an Alfahd compute node (High-Performance Computing facil-
 476 ity at King Fahd University of Petroleum and Minerals) with an Intel Xeon CPU
 477 E5-2680 v4 and 128 GB of memory. The codes are compiled with Intel Fortran
 478 Compiler version 18.0 using `-O3 -xCORE-AVX2` flags. The total number of timesteps
 479 required by the DVM simulations is minimal when $\text{Kn} = 1$, while that required by
 480 the DSBGK method increases with Kn. The DSBGK method requires less than one
 481 minute of CPU time to obtain converged solutions, which is about 2 to 15 times
 482 more expensive than the DVM. However, the **overall** CPU time for a DSBGK sim-
 483 ulation is much longer, about 50 to 80 times higher than that of DVM, due to the
 484 time-averaging process.

485 For large-scale simulations, the efficiency of the DSBGK method should be en-

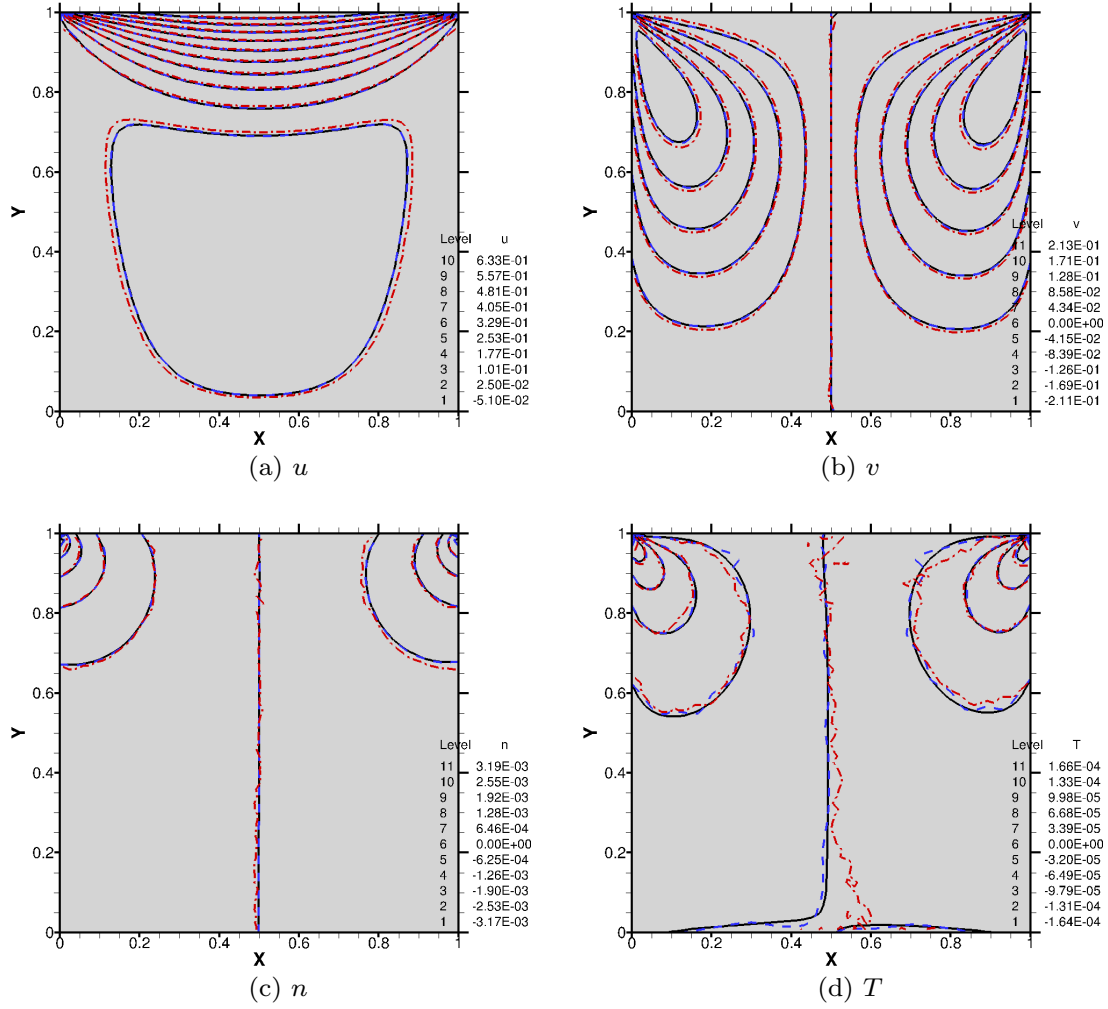


Figure 7: Contours of the perturbed u , v , n and T in the 2D lid-driven cavity flow obtained by the DVM using an 8×80 velocity grid (black solid lines), the DVM using a 4×24 velocity grid (blue dashed lines), and the DSBGK method using 10 simulated molecules per cell with the simple boundary condition and 5000 samples (red dash-dot lines); $Ma = 3.2 \times 10^{-3}$, $Kn = 0.1$.

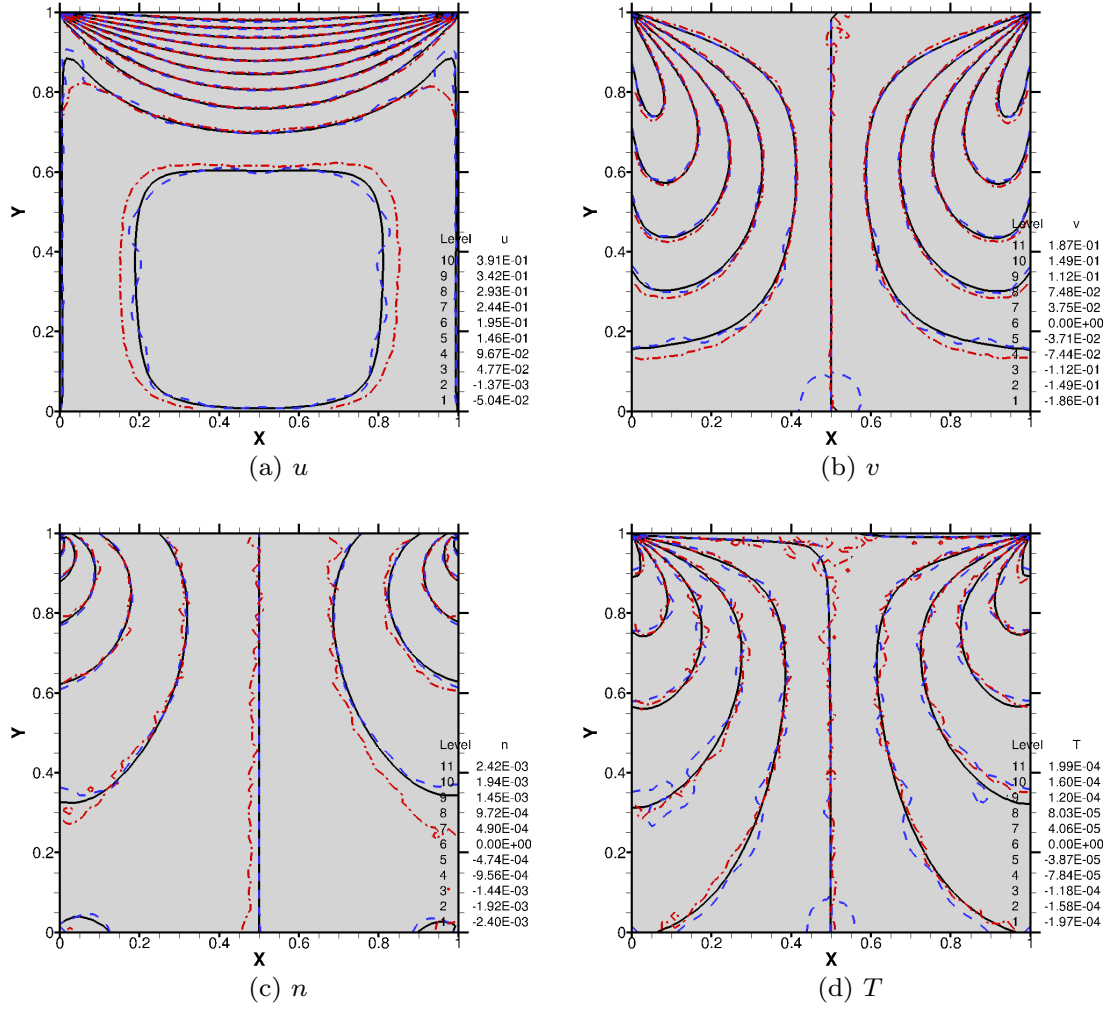


Figure 8: Contours of the perturbed u , v , n and T in the 2D lid-driven cavity flow obtained by the DVM using an 8×80 velocity grid (black solid lines), the DVM using a 4×40 velocity grid (blue dashed lines), and the DSBGK method using 10 simulated molecules per cell with the simple boundary condition and 5000 samples (red dash-dot lines); $Ma = 3.2 \times 10^{-3}$, $Kn = 1$.

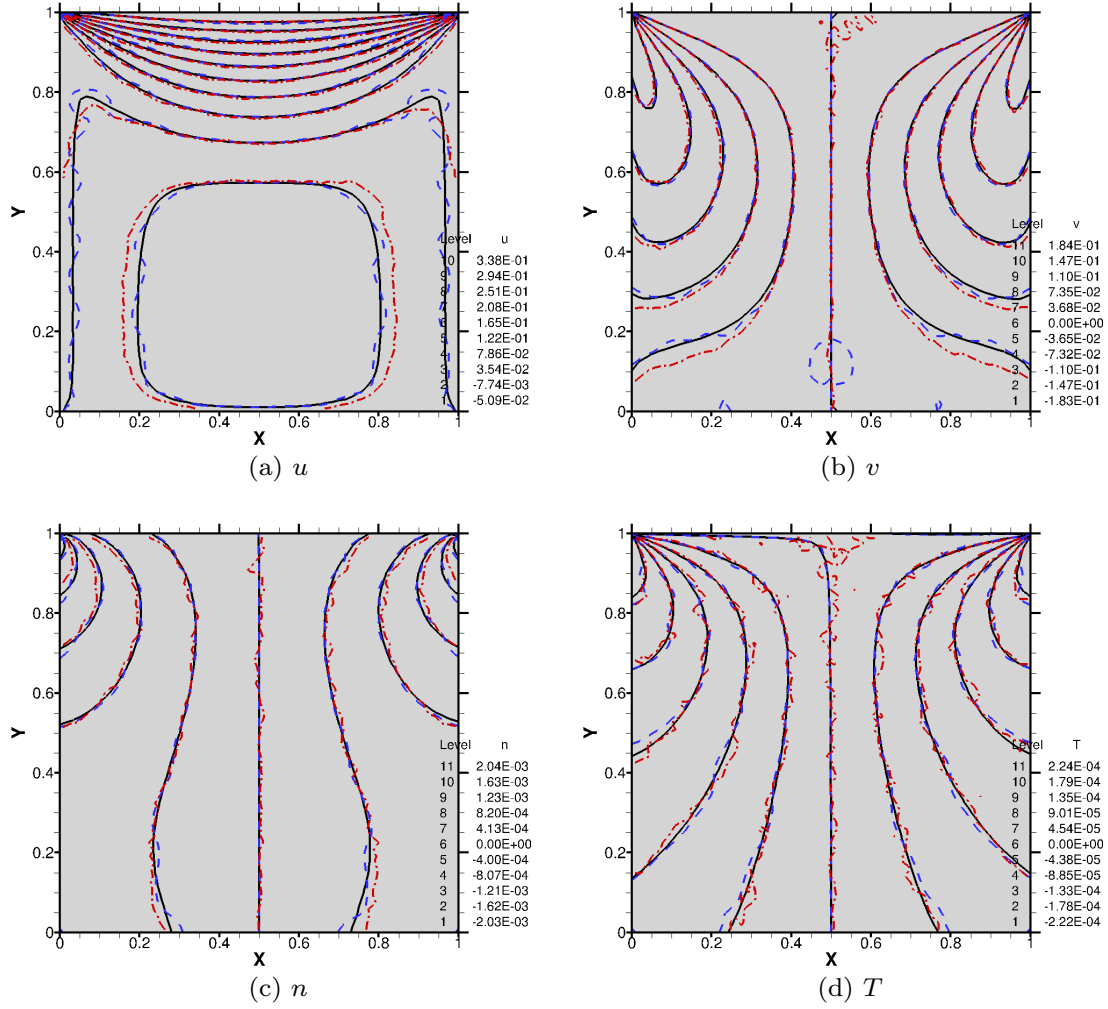


Figure 9: Contours of the perturbed u , v , n and T in the 2D lid-driven cavity flow obtained by the DVM using an 8×80 velocity grid (black solid lines), the DVM using a 4×48 velocity grid (blue dashed lines), and the DSBGK method using 10 simulated molecules per cell with the simple boundary condition and 5000 samples (red dash-dot lines); $Ma = 3.2 \times 10^{-3}$, $Kn = 8$.

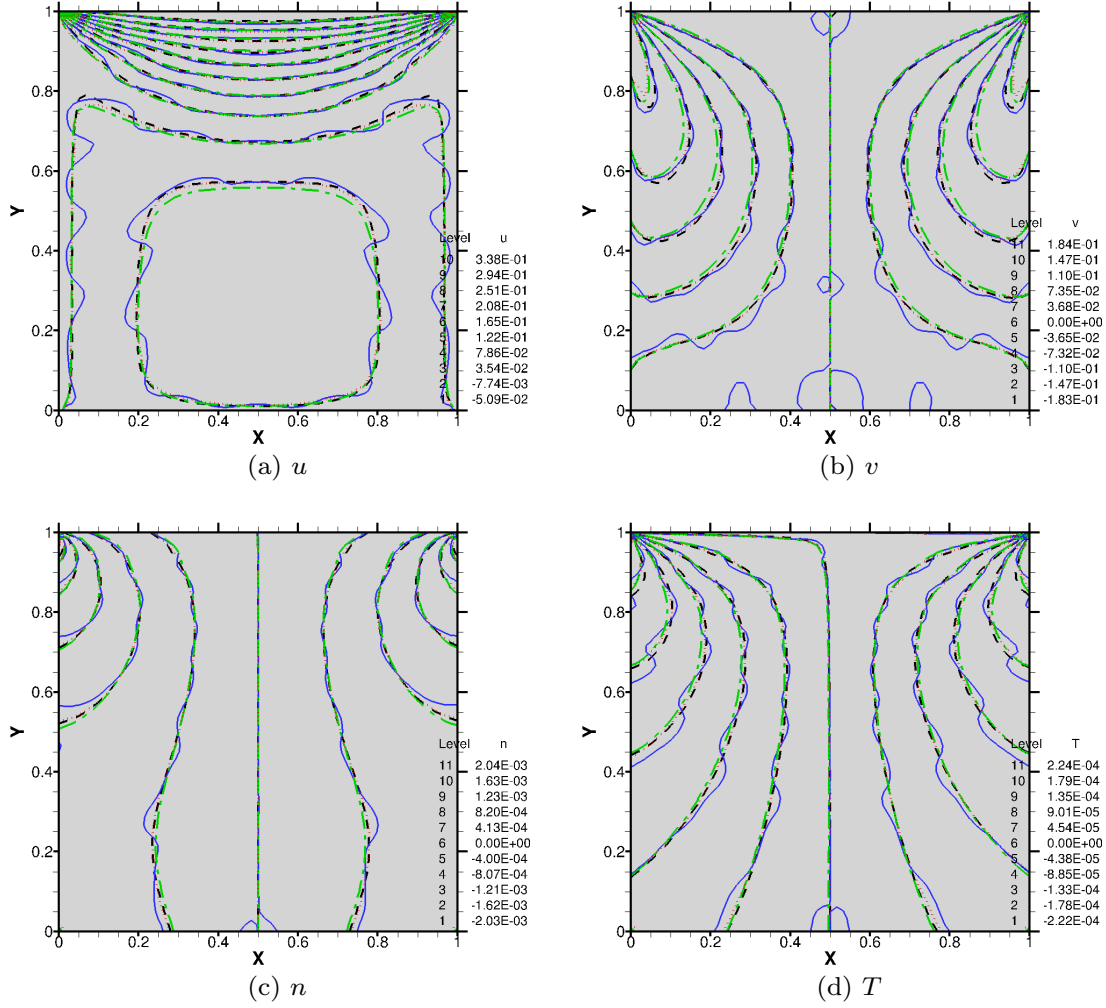


Figure 10: For the 2D flow case with $Ma = 3.2 \times 10^{-3}$, $Kn = 8$, ray effects (wavy contours) in the DVM solution when using a 4×40 velocity grid and a 60^2 spatial grid (blue solid lines) are diminished by increasing the velocity grid to 4×80 (black dash lines) or by decreasing the spatial grid to 30^2 (red dot lines) or by reducing the order of accuracy to a first order upwind scheme (green dash dot line).

Table 1: The computational costs of using the DVM and DSBGK methods in the 2D lid-driven cavity flow problem for $\text{Ma} = 3.2 \times 10^{-3}$ and with 60^2 spatial grids/cells.

Kn	DVM			DSBGK		
	0.1	1	8	0.1	1	8
velocity grids $N_{c_p} \times N_\varphi$	4×24	4×40	4×48	-	-	-
simulated molecules per cell	-	-	-	10	10	10
timesteps for convergence	124	44	51	200	400	1600
timesteps in total	124	44	51	5200	5400	6600
CPU time (s) for convergence	0.97	0.65	1.05	2	4	16
overall CPU time (s)	0.97	0.65	1.05	51	53	65

486 hanced, since the fixed CPU time used for the time-averaging process (i.e. $5000 \Delta t$,
487 as we used here) will become negligible compared to the CPU time needed for con-
488 vergence (e.g. increasing from $200 \sim 1600 \Delta t$ used here to millions of Δt). Thus, the
489 comparison of CPU time required for the convergence process alone is also an impor-
490 tant indicator for large-scale problems. Note also that the comparison of efficiency
491 made here is for this 2D case, where the discretization of velocity space in the third
492 direction is not required in the DVM simulations. Further efficiency comparisons
493 will be made below for the 3D case, where the full 3D velocity grid should be used
494 in DVM.

495 The computational cost can be further reduced by using coarse spatial grids, as
496 long as the cell size is smaller than the mean free path (as in DSMC simulations).
497 We therefore report on how the simulation accuracy is affected when the number
498 of spatial grids/cells reduces from 60^2 to 10^2 , for the case with $\text{Kn} = 1$, $\text{Ma} =$
499 3.2×10^{-2} . Since we focus on the discretization in physical space, high resolution is
500 still maintained in the velocity space here, i.e. the DVM simulation uses an 8×80
501 velocity grid, while the DSBGK simulation employs 2000 simulated molecules per
502 cell and the simple boundary condition.

503 Figure 11 shows the contours of the macroscopic quantities obtained by the
504 DSBGK and DVM methods with the coarse spatial grid. The DVM results using a
505 60^2 spatial grid are also plotted as a reference solution. It can be seen that the n

506 and T contours given by both methods on the coarse spatial grid are in satisfactory
 507 agreement with the reference ones. However, the u and v contours of the coarse
 508 solutions of both methods have some deviations from the reference solutions. This
 509 numerical error is expected to occur also with other simulation methods when using
 510 coarse spatial grids to save computational cost. Balancing computational accuracy
 511 with efficiency becomes a key issue when simulating large-scale problems, e.g. gas
 512 flows in porous media.

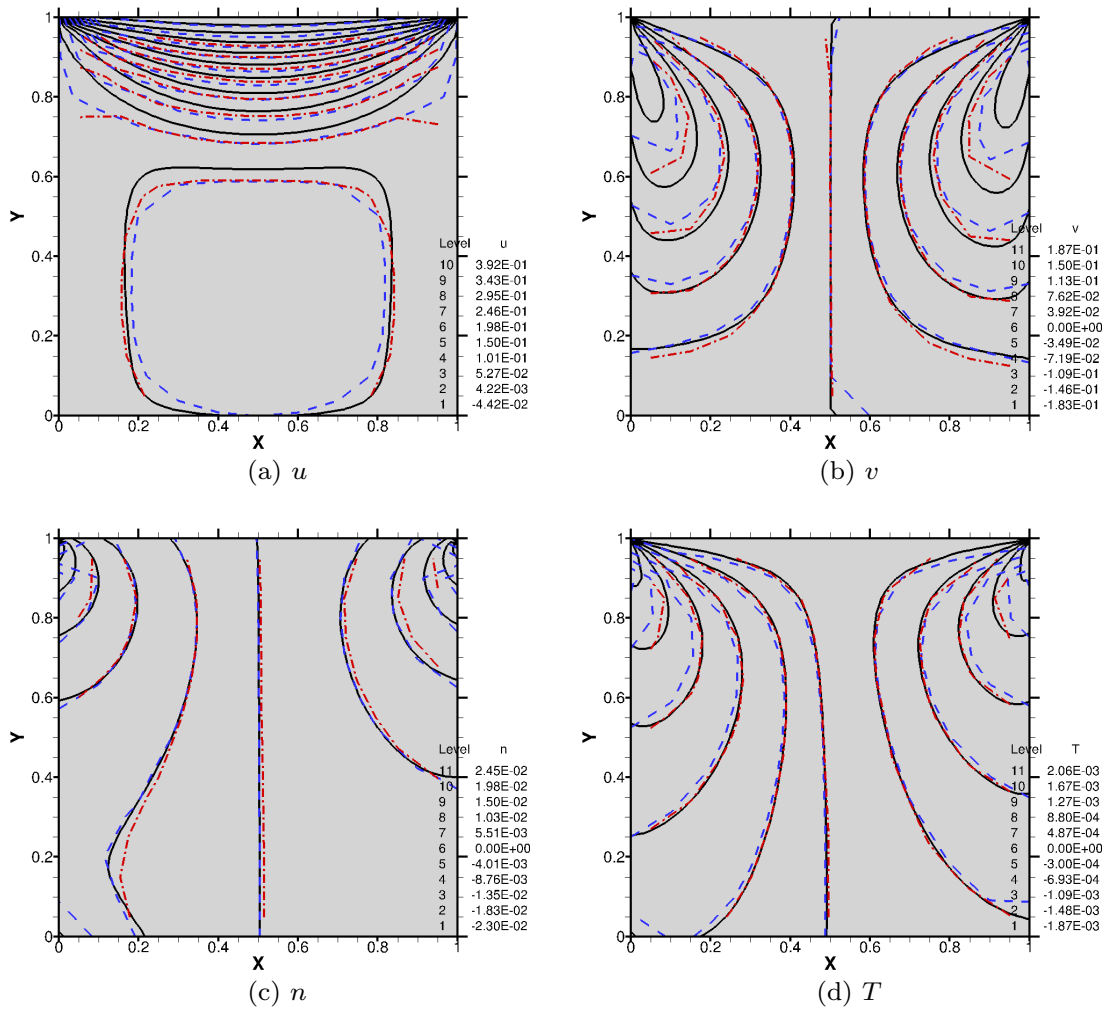


Figure 11: Contours of the macroscopic flow quantities in the 2D lid-driven cavity with $\text{Kn} = 1$ and 3.2×10^{-2} obtained using a 60^2 spatial grid (DVM: black solid lines) and a 10^2 spatial grid (DVM: blue dashed lines, DSBGK: red dash-dot lines).

513 4. 3D cavity flows

514 We now consider the rarefied gas flow inside a cubic cavity of size $L = 1 \mu m$, which is
515 an extension in the Z -direction of the square cavity examined in Section 3. The top
516 lid (in the $X - Z$ plane at $Y = 1$) moves in the positive X -direction with a constant
517 speed u_w , see Fig. 1 (b). We fix $Ma = 3.2 \times 10^{-3}$ and choose $Kn = 0.1, 1$ and 8 , to
518 cover the slip, transition, and free-molecular flow regimes. The number of uniform
519 spatial cells/grids is 60^3 for both the DSBGK and DVM simulations. We use the
520 accurate DVM results as reference data, which are obtained using a $4 \times 80 \times 40$
521 velocity grid.

522 By comparing the u, v, n, T contours on the plane $Z = 0.5$ obtained by the
523 3D reference solutions with those obtained by the 2D reference solutions (shown
524 in Figs. 7-9), the side wall ($Z = 0, 1$) effects on the middle plane are seen to be
525 negligible when $Kn = 0.1$. Although it is not illustrated here, the side wall effects
526 increase with Knudsen number and change the T profiles most significantly.

527 We examine effects of using 10 simulated molecules per cell in the DSBGK
528 method, and coarse velocity grids in the DVM. The coarse DVM grids used in
529 the 2D case are now extended in the inclination θ with $N_\theta = 12$ for this 3D case, i.e.
530 $4 \times 24 \times 12, 4 \times 40 \times 12, 4 \times 48 \times 12$ for $Kn = 0.1, 1, 8$, respectively. The deviations
531 of both methods from the reference solution on the plane $Z = 0.5$ are similar to the
532 2D case. For example, Fig. 12 shows the u, v, n, T contours on the planes $Z = 0.5$
533 and $Y = 0.5$ for the case with $Kn = 8$. The DVM results (left column of Fig. 12)
534 show that although the number of distinct discrete c_z ($N_{c_p} \times N_\theta$) is much less than
535 that of distinct discrete c_x or c_y ($N_{c_p} \times N_\theta \times N_\varphi$), the ray effects (wavy contours)
536 observed in the plane $Y = 0.5$ are less obvious than those in the plane $Z = 0.5$.
537 Moreover, the ray effects in the plane $Y = 0.5$ are more pronounced near the two
538 lateral walls at $Z = 0, 1$. These can be explained by the fact that the discontinuities
539 in wall velocity with respect to the X - and Y -directions exist in all the Z -planes,
540 while those with respect to the Z -direction exist only in the planes $Z = 0, 1$.

541 The serial computational costs of the two numerical methods for the 3D cavity
542 problem, using the same machine as in the 2D cavity problem, are compared in
543 Table 2. Dependence of the number of timesteps on Knudsen number recalls that

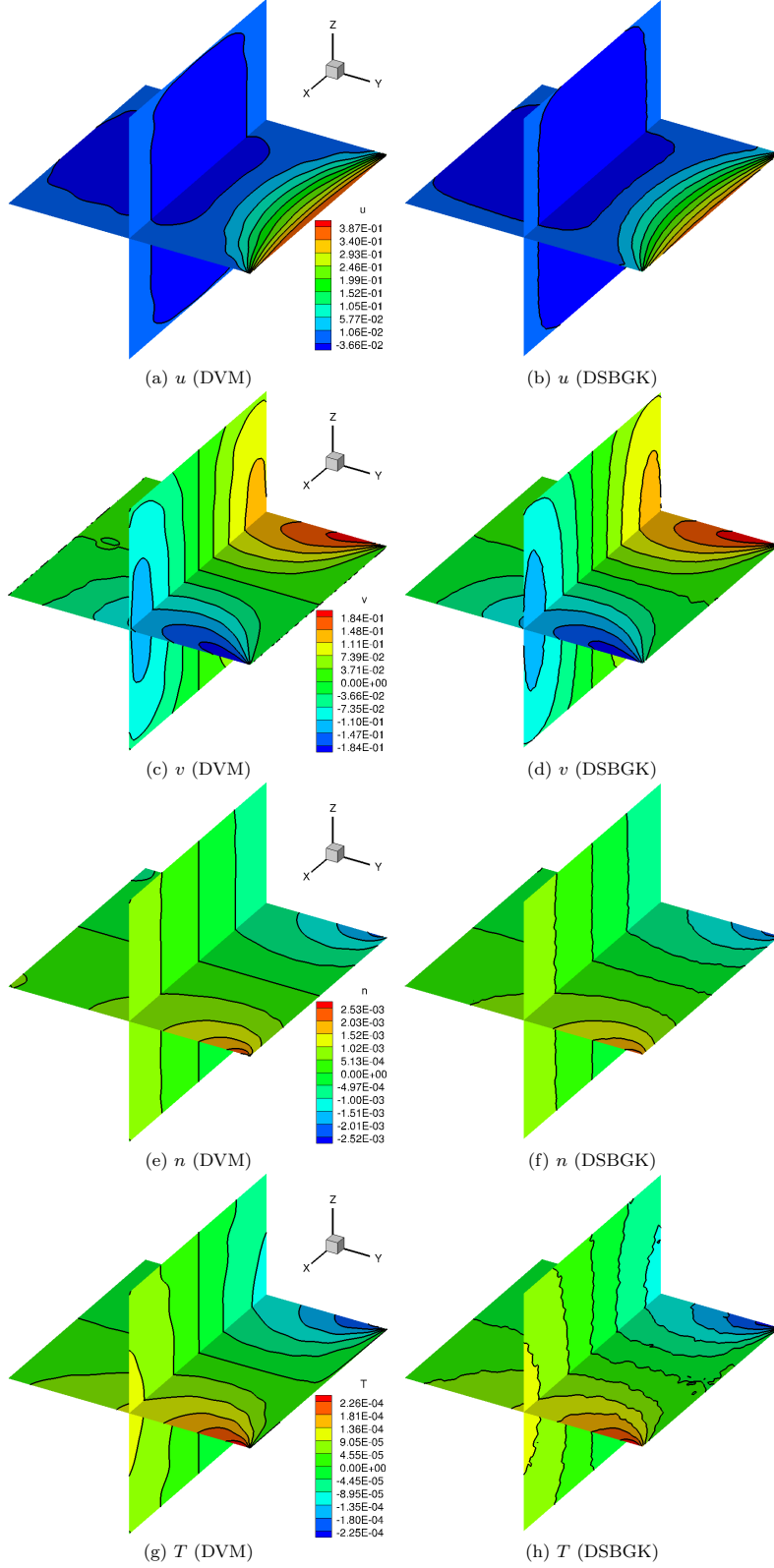


Figure 12: The 3D lid-driven case with $Ma = 3.2 \times 10^{-3}$, $Kn = 8$: contours of the perturbed u , v , n and T on the planes $Z = 0.5$ and $Y = 0.5$, obtained by the DVM using a $4 \times 48 \times 12$ velocity grid (left column), and the DSBGK method using 10 simulated molecules per cell with the simple boundary condition and 5000 samples (right column).

Table 2: The computational costs of using the DVM and DSBGK methods in the 3D lid-driven cavity flow problem for $Ma = 3.2 \times 10^{-3}$ and with 60^3 spatial grids/cells.

Kn	DVM			DSBGK		
	0.1	1	8	0.1	1	8
velocity grids $N_{c_p} \times N_{\varphi} \times N_{\theta}$	$4 \times 24 \times 12$	$4 \times 40 \times 12$	$4 \times 48 \times 12$	-	-	-
simulated molecules per cell	-	-	-	10	10	10
timesteps for convergence	146	67	278	200	400	2400
timesteps in total	146	67	278	5200	5400	7400
CPU time (s) for convergence	1162	882	4473	185	376	2279
overall CPU time (s)	1162	882	4473	4857	5115	7033

544 of the 2D case for both DVM and DSBGK. To reach steady state, the CPU time
545 spent by DVM is about 2 to 6 times more than that needed by the DSBGK method.
546 Including the time-averaging process, however, makes the **overall** computational cost
547 of the DSBGK method from 1.6 to 5.8 times that of the DVM.

548 5. Conclusions

549 We have compared the DVM and DSBGK methods for solving the BGK gas kinetic
550 model applied to low-speed lid-driven cavity flows over a range of Knudsen and Mach
551 numbers. For the 2D case with $Ma = 0.16$, the velocity profiles along the centrelines
552 predicted by the two methods are in good agreement with those reported using
553 the standard DSMC method [37]. When the Mach number decreases, the velocity
554 profiles predicted by the DVM and DSMC methods are essentially independent of
555 Ma , while those of the DSBGK method vary by up to 7.5% (in the u profile) and 2.5%
556 (in the v profile) due to the use of the simple boundary condition. This maximum
557 discrepancy occurs only in the region with relatively small perturbations. Overall,
558 the DVM and DSBGK techniques produce results in good agreement.

559 For 2D case, the magnitudes of the perturbed number density and perturbed
560 temperature in the flow field are observed to increase with the Mach number, while
561 the velocity field remains nearly unchanged. Among the investigated macroscopic
562 quantities, only the temperature distribution is sensitive to the Mach number: the

563 cooler region constrict leftward and expands downward with increasing Mach number
564 while the hotter region expands leftward. For both 2D and 3D cases, the variations
565 of all the macroscopic quantities, except the temperature, reduce significantly with
566 increasing Knudsen number. The regions of low/high number density and temper-
567 ature in the flow field expand with increasing Knudsen number, while the velocity
568 distributions remain unchanged.

569 To reduce the “ray effects” in the DVM simulations that are induced by the
570 discontinuous boundary condition, the velocity grid should be compatible with the
571 spatial grid and the accuracy order of the numerical scheme. With a third-order
572 upwind scheme and a 60^2 spatial grid, the molecular velocity grids of the DVM in
573 2D can be reduced to 4×24 , 4×40 , 4×48 points for $\text{Kn} = 0.1, 1, 8$, respectively, if
574 we accept a maximum local relative error of 10% in the u, v, n, T profiles along the
575 horizontal centreline of the 2D cavity. For the 3D cavity with a 60^3 spatial grid, the
576 corresponding velocity grids of the DVM are $4 \times 24 \times 12$, $4 \times 40 \times 12$, $4 \times 48 \times 12$.

577 Similarly, the number of simulated molecules per cell in the DSBGK method can
578 also be reduced to 10 for all Kn to achieve the same tolerance. The time-averaging
579 process in the DSBGK method needs to be prolonged with decreasing number of
580 simulated molecules per cell to reduce stochastic noise in the solution. This modest
581 number of simulated molecules per cell does, however, result in a much smaller
582 memory requirement for the DSBGK method than for the DVM.

583 The total number of DSBGK timesteps increases with Kn , while the required
584 DVM timesteps are at a minimum at $\text{Kn} = 1$. Compared to a deterministic method
585 like the DVM, the DSBGK method needs additional computational effort for the
586 time-averaging process. For 2D flow problems, the DVM velocity space can also be
587 projected from 3D to 2D to make computational savings. Consequently, the **overall**
588 CPU time consumed by the DSBGK simulations is much larger than that of the
589 DVM in the 2D cavity case, although for the 3D case the computational costs of
590 the two methods become comparable. The efficiency of the DSBGK method can
591 be expected to be enhanced in large-scale 3D simulations, where the required CPU
592 time for time-averaging becomes a negligible part of the overall simulation.

593 **Acknowledgements**

594 This publication is based on work supported by the College of Petroleum Engi-
595 neering and Geosciences, King Fahd University of Petroleum and Minerals, Saudi
596 Arabia. The authors would like to thank the anonymous reviewers for their valuable
597 comments and suggestions to improve the quality of this paper. All data within this
598 publication can be freely accessed at <http://dx.doi.org/>

599 **References**

600 **References**

- 601 [1] C.-M. Ho, Y.-C. Tai, Micro-Electro-Mechanical- Systems (MEMS) and fluid
602 flows, *Annu Rev Fluid Mech* 30 (1998) 579–612.
- 603 [2] H. Darabi, A. Ettehad, F. Javadpour, K. Sepehrnoori, Gas flow in ultra-tight
604 shale strata, *J Fluid Mech* 710 (2012) 641–658.
- 605 [3] G. A. Bird, *Molecular gas dynamics and the direct simulation of gas flows*,
606 Oxford Science Publications, 1994.
- 607 [4] C. Cercignani, *Rarefied Gas Dynamics: From basic concepts to actual calcula-*
608 *tions*, Cambridge University Press, 2000.
- 609 [5] S. Rjasanow, T. Schreiber, W. Wagner, Reduction of the number of particles
610 in the Stochastic Weighed Particle Method for the Boltzmann equation, *J*
611 *Comput Phys* 145 (1998) 382–405.
- 612 [6] A. Crestetto, N. Crouseilles, M. Lemou, Kinetic/fluid micro-macro numerical
613 schemes for Vlasov-Poisson-BGK equation using particles, *Kinet Relat Model*
614 5 (4) (2012) 787–816.
- 615 [7] C. White, T. J. Scanlon, R. E. Brown, Permeability of ablative materials under
616 rarefied gas conditions, *J Spacecr Rockets* 53 (1) (2016) 134–142.
- 617 [8] R. Jambunathan, D. A. Levin, Advanced parallelization strategies using hybrid
618 MPI-CUDA octree DSMC method for modeling flow through porous media,
619 *Comput Fluids* 149 (2017) 70–87.

- 620 [9] G. Yang, B. Weigand, Investigation of the Klinkenberg effect in a mi-
621 cro/nanoporous medium by direct simulation Monte Carlo method, *Phys Rev*
622 *Fluids* 3 (4) (2018) 1–17.
- 623 [10] J. Fan, C. Shen, Statistical simulation of low-speed rarefied gas flows, *J Comput*
624 *Phys* 167 (2) (2001) 393–412.
- 625 [11] L. L. Baker, N. G. Hadjiconstantinou, Variance reduction for Monte Carlo
626 solutions of the Boltzmann equation, *Phys Fluids* 17 (5) (2005) 1–4.
- 627 [12] T. M. M. Homolle, N. G. Hadjiconstantinou, A low-variance deviational simu-
628 lation Monte Carlo for the Boltzmann equation, *J Comput Phys* 226 (2) (2007)
629 2341–2358.
- 630 [13] T. M. M. Homolle, N. G. Hadjiconstantinou, Low-variance deviational simula-
631 tion Monte Carlo, *Phys Fluids* 19 (4) (2007) 041701.
- 632 [14] N. G. Hadjiconstantinou, A. L. Garcia, M. Z. Bazant, G. He, Statistical error
633 in particle simulations of hydrodynamic phenomena, *J Comput Phys* 187 (1)
634 (2003) 274–297.
- 635 [15] P. Bhatnagar, E. Gross, M. Krook, A model for collision processes in gases.
636 I. Small amplitude processes in charged and neutral one-component systems,
637 *Phys Rev* 94 (3) (1954) 511–525.
- 638 [16] G. A. Radtke, N. G. Hadjiconstantinou, Variance-reduced particle simulation of
639 the Boltzmann transport equation in the relaxation-time approximation, *Phys*
640 *Rev E* 79 (5) (2009) 1–9.
- 641 [17] L. Szalmas, Variance-reduced DSMC for binary gas flows as defined by the
642 McCormack kinetic model, *J Comput Phys* 231 (9) (2012) 3723–3738.
- 643 [18] G. Dimarco, L. Pareschi, Hybrid multiscale methods II. Kinetic equations, *Mul-*
644 *tiscale Model Simul* 6 (4) (2008) 1169–1197.
- 645 [19] G. Dimarco, L. Pareschi, Fluid solver independent hybrid methods for multi-
646 scale kinetic equations, *SIAM J Sci Comput* 32 (2) (2010) 603–634.

- 647 [20] P. Degond, G. Dimarco, L. Pareschi, The moment-guided Monte Carlo method,
648 Int J Numer Methods Fluids 67 (2) (2011) 189–213.
- 649 [21] N. Crouseilles, G. Dimarco, M. Lemou, Asymptotically preserving and time
650 diminishing schemes for rarefied gas dynamic, Kinet Relat Model 10 (3) (2017)
651 643–668.
- 652 [22] J. Li, Direct simulation method based on BGK equation, in: Proceedings of
653 the 27th International Symposium on Rarefied Gas Dynamics, Vol. 1333, 2011,
654 pp. 283–288.
- 655 [23] J. Li, Efficiency and stability of the DSBGK method, AIP Conference Proceed-
656 ings 1501 (1) (2012) 849–856.
- 657 [24] J. Li, Comparison between the DSMC and DSBGK methods, arXiv.org
658 physics.co (2012) 1207.1040.
- 659 [25] J. E. Broadwell, Study of rarefied shear flow by the discrete velocity method,
660 J Fluid Mech 19 (3) (1964) 401–414.
- 661 [26] J. Yang, J. Huang, Rarefied flow computations using nonlinear model Boltz-
662 mann equations, J Comput Phys 120 (2) (1995) 323–339.
- 663 [27] K. Aoki, K. Kanba, S. Takata, Numerical analysis of a supersonic rarefied gas
664 flow past a flat plate, Phys Fluids 9 (4) (1997) 1144–1161.
- 665 [28] F. Sharipov, V. Seleznev, Data on internal rarefied gas flows, J Phys Chem Ref
666 Data 27 (3) (1998) 657–706.
- 667 [29] L. Mieussens, Discrete-velocity models and numerical schemes for the
668 Boltzmann-BGK equation in plane and axisymmetric geometries, J Comput
669 Phys 162 (2) (2000) 429–466.
- 670 [30] L. M. Yang, C. Shu, W. M. Yang, J. Wu, An implicit scheme with memory
671 reduction technique for steady state solutions of DVBE in all flow regimes,
672 Phys Fluids 30 (4) (2018) 040901.

- 673 [31] C. K. Chu, Kinetic-theoretic description of the formation of a shock wave, *Phys*
674 *Fluids* 8 (1) (1965) 12–22.
- 675 [32] V. A. Titarev, Conservative numerical methods for model kinetic equations,
676 *Comput Fluids* 36 (9) (2007) 1446–1459.
- 677 [33] A. L. Garcia, W. Wagner, Time step truncation error in direct simulation Monte
678 Carlo, *Phys Fluids* 12 (10) (2000) 2621–2633.
- 679 [34] N. G. Hadjiconstantinou, Analysis of discretization in the Direct Simulation
680 Monte Carlo, *Phys Fluids* 12 (10) (2000) 2634–2638.
- 681 [35] U. Ghia, K. N. Ghia, C. T. Shin, High-Re solutions for incompressible flow
682 using the Navier-Stokes equations and a multigrid method, *J Comput Phys*
683 48 (3) (1982) 387–411.
- 684 [36] S. Naris, D. Valougeorgis, The driven cavity flow over the whole range of the
685 Knudsen number, *Phys Fluids* 17 (9) (2005) 1–12.
- 686 [37] B. John, X. J. Gu, D. R. Emerson, Investigation of heat and mass transfer in
687 a lid-driven cavity under nonequilibrium flow conditions, *Numer Heat Transf*
688 *Part B* 58 (5) (2010) 287–303.
- 689 [38] J. C. Huang, K. Xu, P. Yu, A unified gas-kinetic scheme for continuum and
690 rarefied flows II: Multi-dimensional cases, *Commun Comput Phys* 12 (3) (2012)
691 662–690.
- 692 [39] P. Wang, M. T. Ho, L. Wu, Z. Guo, Y. Zhang, A comparative study of discrete
693 velocity methods for low-speed rarefied gas flows, *Comput Fluids* 161 (2018)
694 33–46.
- 695 [40] H. Babovsky, On a simulation scheme for the Boltzmann equation, *Math Meth-*
696 *ods Appl Sci* 8 (1986) 223–233.
- 697 [41] J. Li, Improved diffuse boundary condition for the DSBGK method to eliminate
698 the unphysical density drift, *arXiv.org physics.co* (2014) 1403.3923.

- 699 [42] M. T. Ho, I. Graur, Heat transfer through rarefied gas confined between two
700 concentric spheres, *Int J Heat Mass Transf* 90 (2015) 58–71.
- 701 [43] B. Shizgal, A Gaussian quadrature procedure for use in the solution of the
702 Boltzmann equation and related problems, *J Comput Phys* 41 (2) (1981) 309–
703 328.
- 704 [44] K. Atkinson, Numerical integration on the sphere, *J Aust Math Soc* 23 (1982)
705 332–347.
- 706 [45] M. T. Ho, I. Graur, Numerical study of unsteady rarefied gas flow through an
707 orifice, *Vacuum* 109 (2014) 253–265.
- 708 [46] L. Wu, J. M. Reese, Y. Zhang, Oscillatory rarefied gas flow inside rectangular
709 cavities, *J Fluid Mech* 748 (2014) 350–367.
- 710 [47] K. D. Lathrop, Ray effects in discrete ordinates equations, *Nucl Sci Eng* 32 (3)
711 (1968) 357–369.
- 712 [48] W. A. Fiveland, Discrete-ordinates solutions of the radiative transport equation
713 for rectangular enclosures, *J Heat Transfer* 106 (4) (1984) 699.
- 714 [49] J. C. Chai, H. O. S. Lee, S. V. Patankar, Ray effect and false scattering in the
715 discrete ordinates method, *Numer Heat Transf Part B* 24 (4) (1993) 373–389.
- 716 [50] P. J. Coelho, The role of ray effects and false scattering on the accuracy of the
717 standard and modified discrete ordinates methods, *J Quant Spectrosc Radiat*
718 *Transf* 73 (2-5) (2002) 231–238.